



HAL
open science

Visible-light High-contrast Imaging and Polarimetry with SCE_xAO/VAMPIRES

Miles Lucas, Barnaby Norris, Olivier Guyon, Michael Bottom, Vincent Deo,
Sébastien Vievard, Julien Lozi, Kyohoon Ahn, Jaren Ashcraft, Thayne Currie,
et al.

► **To cite this version:**

Miles Lucas, Barnaby Norris, Olivier Guyon, Michael Bottom, Vincent Deo, et al.. Visible-light High-contrast Imaging and Polarimetry with SCE_xAO/VAMPIRES. Publications of the Astronomical Society of the Pacific, 2024, 136, 10.1088/1538-3873/ad89af . insu-04836778

HAL Id: insu-04836778

<https://insu.hal.science/insu-04836778v1>

Submitted on 15 Dec 2024

HAL is a multi-disciplinary open access archive for the deposit and dissemination of scientific research documents, whether they are published or not. The documents may come from teaching and research institutions in France or abroad, or from public or private research centers.

L'archive ouverte pluridisciplinaire **HAL**, est destinée au dépôt et à la diffusion de documents scientifiques de niveau recherche, publiés ou non, émanant des établissements d'enseignement et de recherche français ou étrangers, des laboratoires publics ou privés.











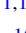

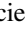
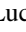
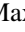
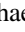


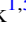



Distributed under a Creative Commons Attribution 4.0 International License



OPEN ACCESS

Visible-light High-contrast Imaging and Polarimetry with SCExAO/VAMPIRES

Miles Lucas¹ , Barnaby Norris^{2,3,4} , Olivier Guyon^{5,6,7,8} , Michael Bottom¹ , Vincent Deo⁵ , Sébastien Vievard^{5,8} ,
Julien Lozi⁵ , Kyohoon Ahn^{5,9} , Jaren Ashcraft⁶ , Thayne Currie^{5,10} , David Doelman^{11,12} , Tomoyuki Kudo⁵ ,
Lucie Leboulleux¹³ , Lucinda Lilley^{2,3} , Maxwell Millar-Blanchaer¹⁴ , Boris Safonov¹⁵ , Peter Tuthill² ,
Taichi Uyama¹⁶ , Aidan Walk^{1,5} , and Manxuan Zhang¹⁴ 

¹ Institute for Astronomy, University of Hawai'i, 640 N. Aohoku Pl., Hilo, HI 96720, USA

² Sydney Institute for Astronomy, School of Physics, Physics Road, University of Sydney, NSW 2006, Australia

³ Sydney Astrophotonic Instrumentation Laboratories, Physics Road, University of Sydney, NSW 2006, Australia

⁴ AAO-USyd, School of Physics, University of Sydney, NSW 2006, Australia

⁵ Subaru Telescope, National Astronomical Observatory of Japan, 650 N. Aohoku Pl., Hilo, HI 96720, USA

⁶ College of Optical Sciences, University of Arizona, Tucson, AZ 85721, USA

⁷ Steward Observatory, University of Arizona, Tucson, AZ 85721, USA

⁸ Astrobiology Center, 2 Chome-21-1, Osawa, Mitaka, Tokyo, 181-8588, Japan

⁹ Korea Astronomy and Space Science Institute, 776 Daedeok-daero, Yuseong-gu, Daejeon 34055, Republic of Korea

¹⁰ Department of Physics and Astronomy, University of Texas at San Antonio, One UTSA Circle, San Antonio, TX 78249, USA

¹¹ Leiden Observatory, Leiden University, P.O. Box 9513, 2300 RA Leiden, The Netherlands

¹² SRON Netherlands Institute for Space Research, Niels Bohrweg 4, 2333 CA, Leiden, The Netherlands

¹³ University Grenoble Alpes, CNRS, IPAG, 38000 Grenoble, France

¹⁴ Department of Physics, University of California, Santa Barbara, CA 93106, USA

¹⁵ Sternberg Astronomical Institute, Lomonosov Moscow State University, 119992 Universitetskii prospekt 13, Moscow, Russia

¹⁶ Department of Physics and Astronomy, California State University, Northridge, Northridge, CA 91330, USA

Received 2024 August 21; accepted 2024 October 17; published 2024 November 8

Abstract

We present significant upgrades to the Visible Aperture-Masking Polarimetric Imager/Interferometer for Resolving Exoplanetary Signatures (VAMPIRES) instrument, a visible-light (600–800 nm) high-contrast imaging polarimeter integrated within SCExAO on the Subaru telescope. Key enhancements include new qCMOS detectors, coronagraphs, polarization optics, and a multiband imaging mode, improving sensitivity, resolution, and efficiency. These upgrades position VAMPIRES as a powerful tool for studying sub-stellar companions, accreting protoplanets, circumstellar disks, stellar jets, stellar mass-loss shells, and solar system objects. The instrument achieves angular resolutions from 17 to 21 mas and Strehl ratios up to 60%, with 5σ contrast limits of 10^{-4} at $0''.1$ to 10^{-6} beyond $0''.5$. We demonstrate these capabilities through spectro-polarimetric coronagraphic imaging of the HD 169142 circumstellar disk, ADI+SDI imaging of the sub-stellar companion HD 1160B, narrowband H α imaging of the R Aqr emission nebula, and spectro-polarimetric imaging of Neptune.

Unified Astronomy Thesaurus concepts: [Direct imaging \(387\)](#); [Polarimetry \(1278\)](#); [Spectropolarimetry \(1973\)](#); [Astronomical optics \(88\)](#); [Astronomical instrumentation \(799\)](#); [Coronagraphic imaging \(313\)](#); [Interferometry \(808\)](#); [Astronomical detectors \(84\)](#); [Visible astronomy \(1776\)](#)


1. Introduction

The advent of 8 m class telescopes combined with the advances in extreme adaptive optics has revolutionized astronomy by enabling high-angular resolution and high-sensitivity imaging and spectroscopy (Guyon 2018; Currie et al. 2023; Galicher & Mazoyer 2024). By employing cutting-edge technologies, innovative observing techniques, and sophisticated post-processing methods, high-contrast imaging (HCI) mitigates the diffraction

effects of the stellar point-spread function (PSF), enabling the study of faint circumstellar signals.

In recent years, the majority of HCI science has occurred at near-infrared (NIR) and thermal-infrared (TIR) wavelengths (1–5 μm) because longer wavelengths are affected less by atmospheric turbulence (Fried 1966; Roddier 1981). Currently, HCI instruments can reach $>90\%$ Strehl ratios, a measure of the PSF quality, in good conditions in the NIR (Beuzit et al. 2019; Lozi et al. 2020b). Stable, high-quality PSFs are required for efficient diffraction control via coronagraphic or interferometric techniques.

High-contrast imaging instruments are more sensitive to optical path differences in visible light than in NIR (Fried 1966;

 Original content from this work may be used under the terms of the [Creative Commons Attribution 3.0 licence](#). Any further distribution of this work must maintain attribution to the author(s) and the title of the work, journal citation and DOI.

Roddiier 1981). Even the most advanced AO systems can only reach 40%–60% Strehl ratios at visible wavelengths (Ahn et al. 2021; Males et al. 2022). This can be mitigated with “lucky imaging”, where images are taken faster than the speckle coherence time ($\tau_0 \sim 4$ ms, Kooten & Izett 2022) “freezing” the speckle pattern, allowing individual frames with high-quality PSFs to be aligned and combined while discarding poor-quality frames (Law et al. 2006; Garrel et al. 2012; Lang et al. 2016).

Despite the challenges in wavefront control, visible-light instruments have some key advantages (Close et al. 2014). Visible wavelengths have a smaller diffraction limit and, therefore, higher angular resolution than the NIR. The sky background is orders of magnitude fainter in the visible. Stellar emission lines in the visible (e.g., $H\alpha$, O III, S II) have much higher contrasts compared to their local continuum than in the NIR (e.g., $Pa\beta$). Visible detectors have better noise characteristics and operational flexibility than infrared detectors, including more compact assemblies, simpler cooling requirements, and lower cost.

Specific science cases for visible HCI include circumstellar disks (Benisty et al. 2023), exoplanet and sub-stellar companions (Hunziker et al. 2020), evolved stars’ atmospheres and mass-loss shells (Norris et al. 2015), stellar jets (Schmid et al. 2017; Uyama et al. 2022), accreting protoplanets (Uyama et al. 2020; Benisty et al. 2021), close binaries (McClure et al. 1980; Escorza et al. 2019), and solar system objects (Schmid et al. 2006; Vernazza et al. 2021).

Visible-light high contrast instruments include SCEXAO/VAMPIRES (Norris et al. 2015), SPHERE/ZIMPOL (Schmid et al. 2018), MagAO-X/VisAO (Males et al. 2024), and LBT/SHARK-VIS (Mattioli et al. 2018). These instruments share some commonalities. They are all deployed on large telescopes with extreme AO correction—high-order deformable mirrors and high framerate, photon-counting wavefront sensors. VisAO, SHARK-VIS, and VAMPIRES use high-framerate detectors for lucky imaging. All instruments have some form of narrowband spectral emission line imaging. Finally, VAMPIRES and ZIMPOL offer polarimetric modes, which use high-speed polarimetric modulation to combat atmospheric seeing.

This work presents significant upgrades to VAMPIRES, improving its capabilities as a high-contrast imager. These upgrades revolved around the deployment of two CMOS detectors with high-framerate photon-number-resolving capabilities, a suite of coronagraphs optimized for the visible, a new multiband imaging mode for simultaneous imaging in multiple filters, and a new achromatic liquid crystal polarization modulator. These upgrades significantly improve VAMPIRES’ high-contrast capabilities, reaching deeper sensitivity limits with improved efficiency.

2. The VAMPIRES Instrument

The Visible Aperture-Masking Polarimetric Imager/Interferometer for Resolving Exoplanetary Signatures (VAMPIRES) is the

visible-light (600–775 nm) sub-instrument of the Subaru Coronagraphic Extreme Adaptive Optics testbed (SCEXAO; Jovanovic et al. 2015b). SCEXAO is a platform for HCI and technology development on the 8.2 m Subaru telescope; the multi-stage adaptive optics achieves diffraction-limited imaging at visible wavelengths, and the large telescope diameter produces angular resolutions of ~ 20 mas. Observing modes and science use cases for VAMPIRES are detailed in Table 1 and a schematic of the optical path for VAMPIRES is shown in Figure 1.

2.1. Telescope and Common Path Instruments

SCEXAO is mounted on one of the Nasmyth platforms of the Subaru telescope. The first common-path instrument is the facility waveplate unit (WPU; Watanabe et al. 2018). The WPU includes a linear polarizer, rotatable half-wave plate (HWP), and rotatable quarter-wave plate (QWP), which is used for polarimetric modulation and calibration (Section 7). Next is Subaru’s facility AO instrument, which provides a first-level atmospheric turbulence correction. It includes a broadband atmospheric dispersion corrector (ADC), visible and NIR wavefront sensors (WFS), and a deformable mirror (DM). A 600 nm longpass dichroic splits light between the WFS (< 600 nm) and downstream instruments (> 600 nm). The results presented in this paper were obtained with a 188-actuator DM used for this stage (AO188; Minowa et al. 2010); it has since been replaced by a 3228-count actuator DM (AO3K; see Section 11.1).

2.2. SCEXAO Common Path

Light entering SCEXAO is corrected with a 2000-actuator DM at up to 3.6 kHz speeds for extreme AO correction (Lozi et al. 2020a; Ahn et al. 2021). SCEXAO operates its DM independently from the facility AO in a cascading way, correcting the residual errors. The corrected beam is split with NIR light sent to a suite of sub-instruments, including CHARIS (Groff et al. 2015), MEC (Steiger et al. 2022), and FastPDI (Lozi et al. 2020b), while visible light is reflected into a periscope and reimaging lens.

A portion of the light exiting the periscope is sent to the visible pyramid WFS (PyWFS; Lozi et al. 2019). Various dichroic and gray beamsplitters are available, but the typical configuration uses an 800 nm shortpass dichroic. The tilt angle of this dichroic ($\sim 20^\circ$) shifts the cut-off wavelength closer to ~ 775 nm. Following this pickoff is a focal plane mount that hosts a $3'' \times 3''$ field stop and a suite of visible coronagraphs (Section 6). Following the field stop are two gray beamsplitters for fiber-fed sub-instruments (Vievard et al. 2023a, 2023b).

2.3. VAMPIRES Optics

The remaining light (600–775 nm) is collimated into a 7.06 mm diameter beam. This beam passes through a

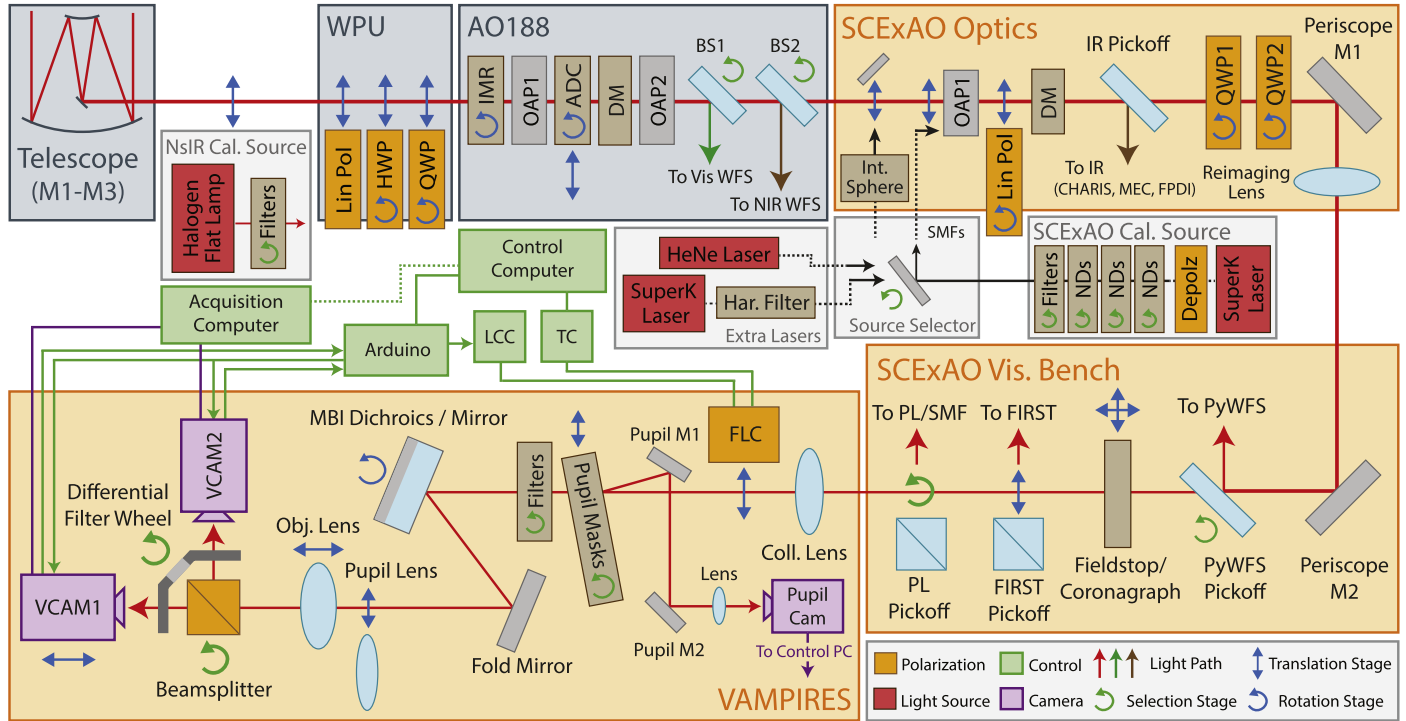


Figure 1. VAMPIRES Instrument Schematic including all common path instruments: the telescope, waveplate unit (WPU), AO188, and SCExAO. Some components are simplified or omitted for clarity and are not to scale. NsIR: Nasmyth infrared platform of the Subaru Telescope, HWP: half-wave plate, QWP: quarter-wave plate, IMR: image rotator (K-mirror), OAP: off-axis parabolic mirror, ADC: atmospheric dispersion corrector, DM: deformable mirror, BS: beamsplitter, PyWFS: pyramid wavefront sensor, PL: photonic lantern, SMF: single-mode fiber, FLC: ferroelectric liquid crystal, LCC: liquid-crystal controller, TC: temperature controller, ND: neutral density filter.

Table 1
VAMPIRES Observing Configurations

Mode	Description	Use Cases
<i>Filters</i>		
Standard	Open, 625-50, 675-50, 725-50, 750-50, 775-50	Highest throughput with Open filter
Multiband	F610, F670, F720, F760	Spectral differential imaging, color analysis, phase diversity
Narrowband	H α , H α -Cont, S II, S II-Cont	Narrowband spectral differential imaging, accreting proto-planets, stellar jets, stellar atmospheres
<i>Polarimetry</i>		
Fast polarimetry	Triple-difference with HWP+FLC (DIT < 1 s)	Circumstellar disks, sub-stellar companions, stellar atmospheres, stellar jets, solar system objects
Slow polarimetry	Double-difference with HWP	Circumstellar disks, stellar jets, solar system objects
<i>Coronagraphy</i>		
No coronagraph	5σ contrast: 10^{-3} at $0''.1$, 10^{-4} at $>0''.4$	Stellar companions, circumstellar disks (with PDI), solar system objects
Classic Lyot	IWA: 37, 59, 105, or 150 mas; 5σ contrast: 10^{-4} at $0''.1$, 10^{-6} at $>0''.5$	Sub-stellar companions and circumstellar disks
Vector vortex	IWA: 61 mas; 5σ contrast: TBD (not compatible with polarimetry)	Sub-stellar companions and circumstellar disks
<i>Aperture masking</i>		
NRM interferometry	7, 9, and 18-hole non-redundant masks, plus a redundant annulus mask (not compatible with coronagraphs)	Dust shells, stellar atmospheres, circumstellar disks
Redundant apodizing pupil	8–35 λ/D dark hole resilient to <1 rad of low-wind effect (not compatible with coronagraphs)	Circumstellar disks and sub-stellar companions

removable ferroelectric liquid crystal (FLC), a pupil mask wheel, and a filter wheel. The pupil wheel houses sparse aperture masks, neutral-density (ND) filters, and the coronagraphic Lyot stops. This wheel is tilted at $\sim 6^\circ$ so that a separate pupil-viewing camera can image light reflected off the masks. The standard filter wheel houses five 50 nm wide bandpass filters for standard imaging and an empty slot for broadband observations. After the filter wheel is a baffle isolating the VAMPIRES fore-optics.

Next, the beam reaches the multiband imaging optics and the VAMPIRES objective lens. A pupil-imaging lens can be inserted with a flip mount. As the beam converges, it passes the beamsplitter wheel, which hosts a wire-grid polarizing cube and a gray non-polarizing cube. The beamsplitters can be removed for single-camera operation. The last device before the detectors is a differential filter wheel that swaps narrowband filters between each camera for narrowband spectral differential imaging (Uyama et al. 2020). The two VAMPIRES detectors are described in detail in Section 3.

2.4. Multiband Imaging

One of the main goals of the VAMPIRES upgrades was enabling spectral differential imaging (SDI) without adding dispersive optics. Dispersive optics, like in an integral-field unit (IFU), require space for a prism or grating, lenslets, and reimaging optics. Space is limited in VAMPIRES to only ~ 20 cm after the pupil mask. We developed a technique for “low-resolution dispersion” using dichroic filters to form multiple images in a compact assembly called multiband imaging (MBI).

The MBI technique is enabled by using multiple dichroics with unique angles-of-incidence (AOI) to split broadband collimated light into multiple fields imaged on the detector (Figure 2). This approach takes advantage of the large sensor size of the detectors, which only uses 3% of the detector for a $3'' \times 3''$ field of view (FOV)—up to four FOVs can be tiled side-by-side before the objective lens starts to distort the off-axis images, which still only uses half the available detector area.

The optical design comprises three shortpass dichroic filters (750 nm, 700 nm, and 650 nm) plus a protected silver mirror to create four ~ 50 nm bandpass fields (Figure 6). The assembly can be rotated 180° to become a fold mirror. A $\sim 10^\circ$ protected silver fold mirror redirects the beam(s) towards the objective lens.

Ghost images are produced by repeated reflections between dichroic surfaces, which interfere with high-contrast observations. The geometry of the dichroic tilt angles was optimized so that all ghost images fall completely outside of the FOVs of the primary fields (Appendix D). Field stops are required to avoid overlap between fields, and all coronagraph masks include a field stop.

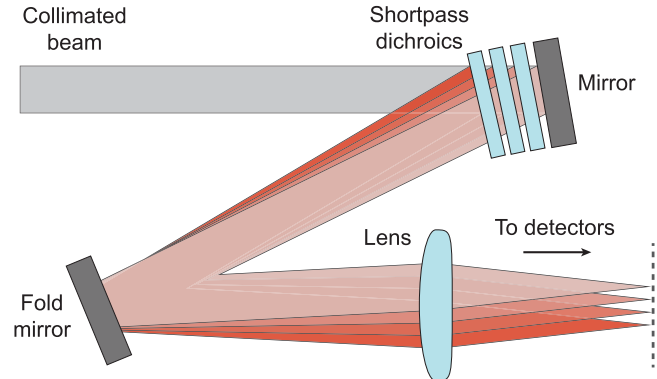


Figure 2. Schematic drawing of the multiband imaging principle. Broadband collimated light reaches the stack of tilted dichroics and mirrors. Light reflected by each dichroic creates a unique field in the focal plane due to the angle of incidence, transmitting the remaining bandpass onto the next dichroic. The final mirror reflects all remaining light through the stack.

The required precision of the MBI dichroic tilt angles is on the order of $\sim 3''$ to ensure neighboring fields do not overlap. This corresponds to a linear precision of $\sim 1 \mu\text{m}$ along the circumference of the 25 mm diameter, which is ~ 100 times finer than standard machining tolerances. Precision manufacturers NH Micro¹⁷ created titanium ring spacers and a custom lens tube using electrical-discharge machining, which has $\sim 1 \mu\text{m}$ tolerances. When fully assembled, the spacers self-align in the lens tube, and interferometric analysis shows no optical distortions of the wavefront.

3. Detectors

Fast, low-noise detectors are a key component for HCI, and a major component of the VAMPIRES upgrades revolved around improving the detectors. Previously, VAMPIRES used two Andor iXon Ultra 897 EMCCDs.¹⁸ Through electron multiplication, the effective rms read noise can be lowered to $\sim 0.27e^-$, but the dynamic range is limited (64 dB). In addition, the Andor detectors have a maximum framerate of 56 Hz, which is not fast enough to freeze the atmospheric speckles, which evolve on timescales of ~ 1 ms above Maunakea (Kooten & Izett 2022).

We upgraded VAMPIRES by replacing the two Andor EMCCDs with Hamamatsu ORCA-Quest qCMOS detectors.¹⁹ The qCMOS detectors were chosen for their fast readout (~ 500 Hz at 536×536), low read noise (~ 0.25 – $0.4e^-$ rms), and high dynamic range (~ 85 – 90 dB). The new detectors have two readout modes: “fast” and “slow” mode. In “fast” mode the rms read noise is $0.4e^-$ and the allowed detector integration

¹⁷ <https://www.nhmicro.com/>

¹⁸ <https://andor.oxinst.com/products/ixon-emccd-camera-series/ixon-ultra-897>

¹⁹ <https://www.hamamatsu.com/us/en/product/cameras/qcmos-cameras/C15550-20UP.html>

Table 2
VAMPIRES Detector Characteristics

Parameter	qCMOS		EMCCD	
	fast	slow	$g = 1$	$g = 300$
Gain (e^-/adu)	0.103	0.105	4.5	4.5
rms read noise (e^-)	0.40	0.25	9.6	0.27
Dark current ($e^- \text{ s}^{-1} \text{ px}^{-1}$)	3.6×10^{-3}		1.5×10^{-4}	
Saturation limit ^a (e^-)	6730	6860	1.5×10^5	980
Dyn. range ^b (dB)	85	90	84	71
Max framerate ^c (Hz)	506	21	56	56
Pixel size (μm)	4.6		16	
Ave. QE ^d (%)	67		85	

Notes.

^a The qCMOS full well is larger than the bit-depth, so the saturation limit is the maximum input signal per pixel that can be recorded without clipping.

^b The input-referred dynamic range is derived from the saturation limit divided by the readout noise.

^c Maximum framerate for a 512×512 pixel window.

^d Averaged over VAMPIRES bandpass (600–800 nm).

times (DIT) are $7.2 \mu\text{s}$ – 1800 s with a maximum framerate of 506 Hz for a $3'' \times 3''$ FOV crop. In “slow” mode the rms read noise is $\sim 0.25e^-$, but the DIT is limited to $>48 \text{ ms}$ (21 Hz). The detectors have rolling-shutter readout, which causes the pixel rows to have slightly different acquisition times. This effect is exacerbated at the fastest exposure times using the electronic shutter. Detailed analysis of the rolling shutter effect is left for future work.

The imaging fore-optics were redesigned to accommodate the smaller detector pixel pitch ($4.6 \mu\text{m}$ now versus $16 \mu\text{m}$ previously), which made the F-ratio faster (F/21 now versus F/52 previously).

3.1. Detector Characterization

To determine the conversion between detector counts and electrons, we measured photon transfer curves using a calibration flat field source for both detectors in both readout modes. The fixed-pattern noise was removed through frame-differencing, and then a linear model was fit to the average signal and the signal variance (Janesick 2007; Stefanov 2022)

$$\sigma^2(\mu|k, \sigma_{\text{RN}}) = \frac{\mu}{k} + \sigma_{\text{RN}}^2. \quad (1)$$

where μ is the average intensity in adu, k is the gain in e^-/adu , and σ_{RN} is the rms read noise in adu.

The detector characteristics are reported in Table 2. The readout noise per pixel was measured from the standard deviation of multiple bias frames and combined in quadrature to derive the rms read noise. The detector photoresponse has nonlinearities at low flux levels and around 2^{13} adu where the junction of 12-bit ADCs occurs (see Strakhov et al. 2023). The

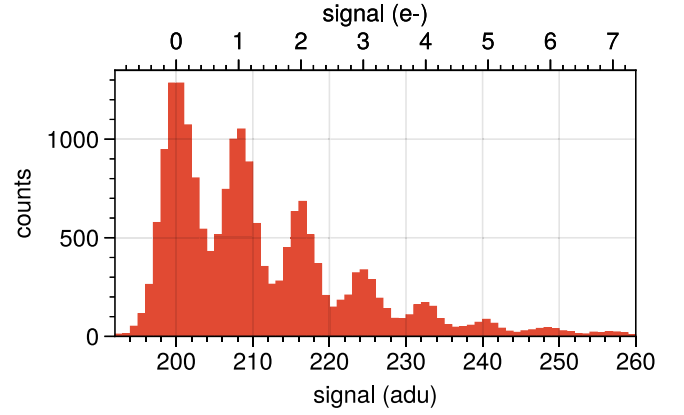


Figure 3. Histogram of 10^4 pixels from a long exposure in “slow” mode ($\sigma_{\text{RN}} = 0.22e^-$). All signals are due to dark current. The Poisson photon number peaks are resolved.

nonlinearities can be corrected to less than 1% with an approximated function. The signal clips at 2^{16} adu, which is less than the full-well capacity of $7000 e^-$ ($\sim 67,000$ adu). The detector dark current is $3.6 \times 10^{-3} e^- \text{ s}^{-1} \text{ px}^{-1}$ at sensor temperatures of -45°C to -40°C .

3.2. Photon Number Resolution

Since the qCMOS detectors have read noise below $\sim 0.3e^-$, they can resolve photon numbers, unambiguously detecting the number of individual photons hitting each pixel (Starkey & Fossum 2016). The photon number statistic is free from frame-to-frame noise (like readout noise) but requires accurate bias subtraction and flat-fielding for practical use. A derivation of the signal-to-noise ratio (S/N) gained by photon number counting is in Appendix C. Photon number resolution is demonstrated in Figure 3, which shows a histogram of 10^4 pixels from a long exposure dark frame. The photon peaks from Poisson statistics are resolved. The method from Starkey & Fossum (2016) was used to determine the gain and quanta exposure directly from the histogram peaks, consistent with results from the photon transfer curves.

3.3. qCMOS versus EMCCD

The relative sensitivity of the qCMOS detectors compared to the previous EMCCDs is shown in Figure 4. The number of detected photoelectrons is

$$S_e = f \cdot t \cdot \text{QE}, \quad (2)$$

where f is the photon flux, t is the detector integration time, and QE is the bandpass-averaged quantum efficiency. Dark-current (f_{DC}) is included for both detectors, which is only a factor of

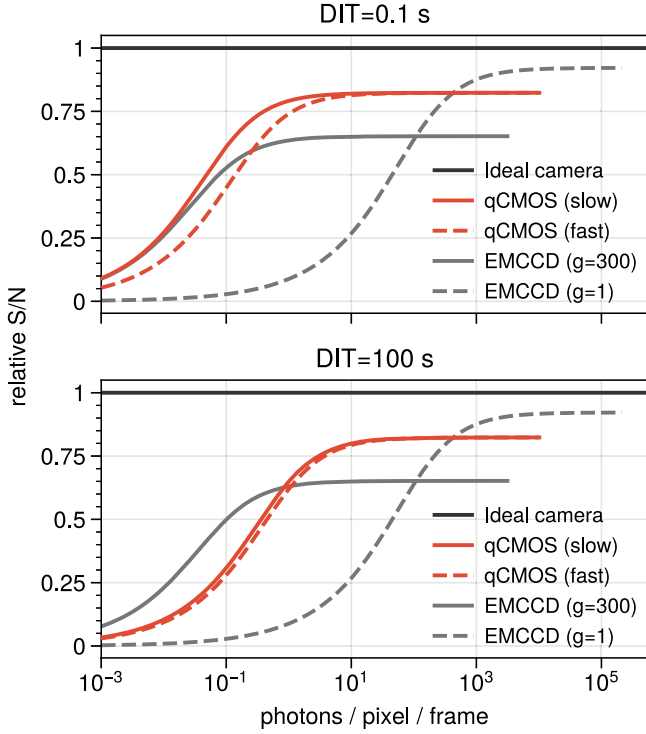


Figure 4. Theoretical normalized S/N curves for the new CMOS detectors (red curves) and the previous EMCCD detectors (gray curves). The curves are normalized to an ideal camera (only photon noise with perfect QE; black curve). The top plot shows a read noise-limited case, and the bottom plot shows a dark-limited case. Noise terms include read noise, dark noise, photon noise, and CIC plus excess noise factor for the EMCCDs.

exposure time—

$$D_e = f_{DC} \cdot t. \quad (3)$$

The S/N per frame for the qCMOS detectors contains shot noise, dark current, and read noise (Janesick 2007; Stefanov 2022)—

$$S/N_{\text{CMOS}} = \frac{S_e}{\sqrt{S_e + D_e + \sigma_{\text{RN}}^2}}, \quad (4)$$

where σ_{RN} is the rms read noise.

For the EMCCDs, extra noise terms unique to the electron-multiplication process (Harpsoe et al. 2012) are incorporated into

$$S/N_{\text{EMCCD}} = \frac{S_e}{\sqrt{(S_e + D_e + f_{\text{CIC}}) \cdot \gamma^2 + (\sigma_{\text{RN}}/g)^2}}, \quad (5)$$

where g is the EM gain, γ is the excess noise factor ($\sqrt{2}$ with EM gain), and f_{CIC} is the clock-induced charge (CIC). CIC of $10^{-3}e^- \text{px}^{-1} \text{frame}^{-1}$ was used based on empirical tests, and vendor values were used for everything else.

The qCMOS detectors have an order of magnitude worse dark current and slightly worse QE than the EMCCDs. Despite this, Figure 4 shows that the qCMOS detectors perform better than the EMCCDs over a broad range of illuminations,

especially at low-light levels. The qCMOS detectors are limited by the dark current shot noise at ~ 15 s in “slow” mode, where the relative performance in the low-flux regime drops compared to the EMCCDs. In practice, though, the sky background is the limiting noise term at these exposure times, which has a larger effect on the S/N for the EMCCDs due to excess noise. Using the EMCCDs without electron multiplication is superior at high photon fluxes due to the lack of excess noise factor (compared to the EMCCD) combined with higher QE (compared to the qCMOS).

3.4. Astrometric Calibration

Previously, Currie et al. (2022) derived a plate scale of $6.24 \pm 0.01 \text{ mas px}^{-1}$ and parallactic angle offset of $(78.6 \pm 1.2)^\circ$ using a single epoch of observations of HD 1160B. However, the changes in optics and detectors, in combination with the non-telecentricity of VAMPIRES (Appendix E), prompted a new astrometric calibration for VAMPIRES. We derive a new astrometric solution for each of the new detectors using a variety of binary star observations.

We observed six binary systems (Albireo, 21 Oph, HD 1160, HIP 3373, HD 137909, and HD 139341) with separations from $0''.12$ to $1''.1$ (Table 3, Figure 5). The uncertainty in plate scale and position angle was dominated by the statistical uncertainty of the ephemerides rather than centroid precision. The observations of HD 1160 only used VCAM1 and were complicated by the process of PSF subtraction, which was required to detect the low-mass companion (see Section 10.2 for more details).

The derived instrument plate scale and parallactic angle offset are shown in Table 4. The instrument angle is defined as the pupil rotation of VAMPIRES to the image rotator zero point, which is calculated by

$$\theta_{\text{inst}} = \theta_{\text{off}} + 180^\circ - \theta_{\text{PAP}}, \quad (6)$$

where θ_{PAP} is the image rotator pupil offset of -39° (to align with the SCEXAO entrance pupil). There is a 180° change in position angle due to a parity flip compared to the previous astrometric solution for VAMPIRES (Currie et al. 2022).

Each camera was characterized separately with and without the multiband imaging dichroics (MBI), but there were no significant differences between the modes. Still, observers with the highest astrometric requirements should observe calibration targets during their run.

4. Filters and Instrument Throughput

4.1. Spectral Filters

VAMPIRES has five 50 nm bandpass filters, four narrow-band filters, an open broadband filter, and the dichroic filters in the multiband optic. All spectral filter transmission curves are compiled from manufacturer data and are shown in Figure 6. The filter characteristics and zero points are summarized in Table 5.

Table 3
Visual Binary Ephemerides Used for Astrometric Calibration

Object	t_{obs} (UT)	ρ (mas)	θ ($^{\circ}$)	References
Albireo	2023/06/27	310.0 ± 7.7	45.1 ± 6.2	(1)
21 Oph	2023/07/08	801 ± 39	-53.0 ± 3.1	(2), (3)
HD 1160	2023/07/11	794.4 ± 8.2	244.30 ± 0.39	(4)
HIP 3373	2023/07/30	393 ± 19	-0.7 ± 3.1	(5)
HD 137909	2024/04/30	124.91 ± 0.81	-166.00 ± 0.23	(6)
HD 139341	2024/04/30	1131.9 ± 3.0	178.15 ± 0.24	(6)

Note. Separation (ρ) and position angle (East of North, θ) are reported for the average observation time of the data.

References. (1): Drimmel et al. (2021), (2): Docobo & Ling (2007), (3): Docobo & Ling (2017), (4): Bowler et al. (2020) (5): Miles & Mason (2017), (6): Muterspaugh et al. (2010), (6): Izmailov (2019).

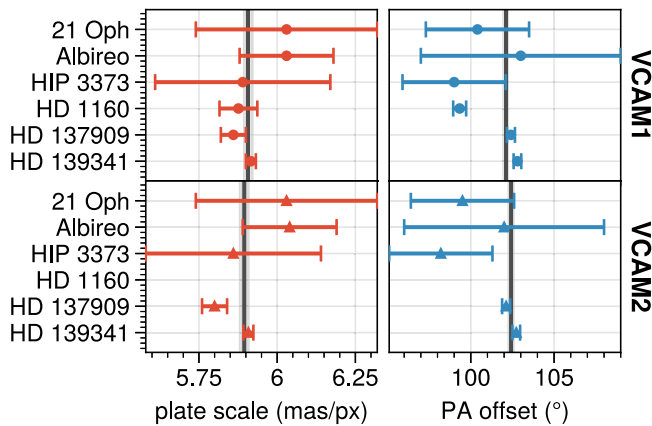


Figure 5. Results of astrometric characterization from each calibrator system shown as the mean with 1σ error bars. The weighted mean and standard error of the weighted mean are shown with a gray vertical line and shaded contours. There are no VCAM2 data for HD 1160.

Table 4
Astrometric Characteristics of VAMPIRES

Cam	Pix. Scale (mas px $^{-1}$)	θ_{off} ($^{\circ}$)	θ_{inst} ($^{\circ}$)
VCAM1	5.908 ± 0.014	102.10 ± 0.15	-38.90 ± 0.15
VCAM2	5.895 ± 0.015	102.42 ± 0.17	-38.58 ± 0.17

Note. The values and uncertainties are the variance-weighted mean and standard error from six observations (Figure 5).

The Open filter is the widest and is constrained by the AO188 beamsplitter and the PyWFS pickoff. The multiband filters are defined by the consecutive transmissions/reflections through the stack of dichroics. The effective bandpasses are ~ 50 nm wide and have spectral leakage ($< 5\%$) between some fields due to the imperfect dichroic transmissions. The narrowband filters come in pairs to enable differential imaging of the emission line and the local continuum. The $H\alpha$ filter is

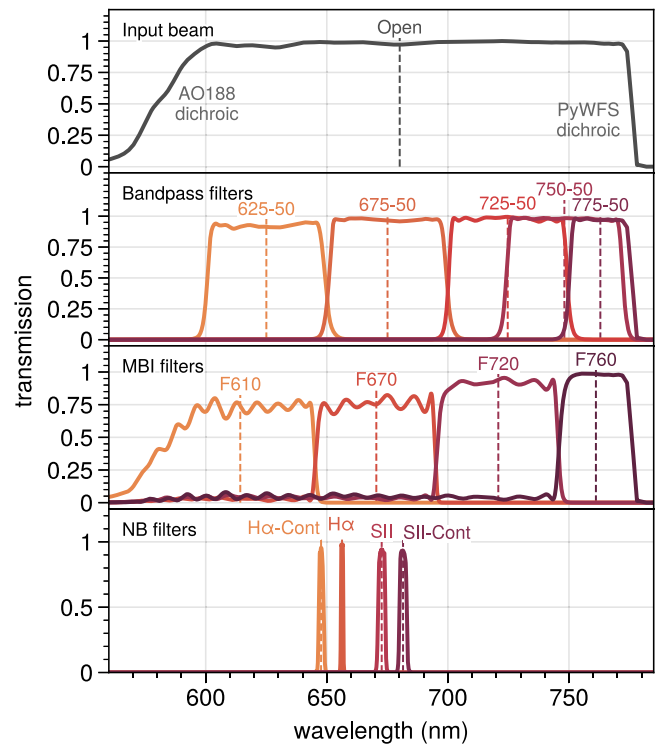


Figure 6. VAMPIRES filter transmission curves. All curves are normalized to the Open filter, the bandpass created from the dichroics upstream of VAMPIRES. The average wavelength for each filter is shown with a vertical dashed line.

1 nm wide and the $H\alpha$ -continuum filter is 2 nm wide. The S II doublet and continuum filters are both 3 nm wide.

4.2. Neutral Density Filters

Two broadband reflective neutral density filters in the pupil mask wheel of VAMPIRES can be used to avoid saturating bright stars. Because these masks are in the pupil wheel, they cannot be used simultaneously with sparse aperture masks or Lyot stops. The optical density was measured for both filters: the ND10 has an optical density of 1.0, and the ND25 has an

Table 5
VAMPIRES Filter Information

Filter	λ_{ave} (nm)	$\lambda_{\text{min}} - \lambda_{\text{max}}$ (nm)	FWHM (nm)	k (mag/airmass)	Through. (%)	QE _{ave} (%)	Zero Points			C _{FD} (Jy s/e ⁻)
							(mag)	(e ⁻ s ⁻¹)	(Jy)	
Open	680	580–776	196	0.06	6.1	68	25.8	2.2×10^{10}	3550	1.6×10^{-7}
625–50	625	601–649	49	0.08	5.1	74	24.3	5.3×10^9	3440	6.6×10^{-7}
675–50	675	651–699	49	0.05	8.6	67	24.6	7.0×10^9	2990	4.3×10^{-7}
725–50	725	700–749	49	0.04	11.7	61	24.7	7.9×10^9	2800	3.6×10^{-7}
750–50	748	724–776	48	0.03	13.0	58	24.7	7.7×10^9	2680	3.6×10^{-7}
775–50	763	750–776	26	0.03	7.3	57	23.2	2.1×10^9	2610	1.6×10^{-6}
Multiband										
F610	614	580–645	65	0.09	3.0	77	24.0	3.9×10^9	4810	1.2×10^{-6}
F670	670	646–695	49	0.06	7.4	68	24.3	5.2×10^9	3150	6.1×10^{-7}
F720	721	696–745	50	0.04	9.2	62	24.6	6.7×10^9	2920	4.4×10^{-7}
F760	761	746–776	30	0.03	6.0	57	23.6	2.7×10^9	2830	1.0×10^{-6}
Narrowband										
H α	656.3	655.9–656.7	0.8	0.06	5.5	69	19.6	7.2×10^7	2170	3.3×10^{-5}
H α -Cont	647.7	646.7–648.6	1.9	0.07	6.0	70	20.9	2.3×10^8	3210	1.4×10^{-5}
S II	672.7	671.2–674.1	2.9	0.05	10.8	67	21.8	5.5×10^8	3090	5.7×10^{-6}
S II-Cont	681.5	680.0–683.0	3.0	0.05	8.9	66	21.6	4.3×10^8	3040	7.0×10^{-6}

Note. λ_{ave} : average wavelength, λ_{min} : minimum wavelength with at least 50% throughput, λ_{max} : maximum wavelength with at least 50% throughput, FWHM: full width at half-maximum, k : average atmospheric extinction from Buton et al. (2013), Through: estimated instrument throughput (includes: telescope, excludes: beamsplitter, FLC, atmosphere), QE_{ave}: average detector quantum efficiency, C_{FD}: flux density conversion factor. Zero points are in Vega magnitudes and map to instrument flux without a beamsplitter in e⁻ s⁻¹. Zero points, instrument throughput, and conversion factors were estimated from spectrophotometric standard stars. All values assume there is no beamsplitter.

optical density of 2.33. The polarimetric effects of these filters have not been characterized and they are not recommended for use during polarimetric observations.

4.3. Beamsplitter Throughput

VAMPIRES has two beamsplitters: a wire-grid polarizing beamsplitter cube (PBS) and a non-polarizing beamsplitter cube (NPBS). The beamsplitter throughput was measured in the Open filter and compared to the flux without a beamsplitter (Table 6). To avoid polarization biases, a linear polarizer was inserted after the internal source and rotated in steps of 5° from 0° to 180°, taking the average value from this range as the throughput.

4.4. Filter Color Corrections

The filters in VAMPIRES do not follow any standard photometric system, although the Open filter is similar in central wavelength and width to the Johnson-Cousins R band (Bessell 1979). When using photometric values from online catalogs, the magnitudes must be converted from the source filter into the respective VAMPIRES filter, which depends on the spectrum of the observed star.

The Pickles stellar models (Pickles 1998) were used to measure the color correction for varying spectral types of main-sequence stars. For each model spectrum, `pysynphot` was used to calculate the color correction in Vega magnitude from Johnson-

Table 6
VAMPIRES Beamsplitter Throughput Measurements

Name	Throughput (%)		
	VCAM1	VCAM2	Sum
Open	100	...	100
PBS	36.76 ± 0.04	42.88 ± 0.04	79.64 ± 0.06
NPBS	43.95 ± 0.04	45.35 ± 0.04	89.31 ± 0.07

Note. PBS: Polarizing beamsplitter, NPBS: Non-polarizing beamsplitter.

Cousins V , R , and Gaia G to the respective VAMPIRES filter (Figure 7). The Johnson V filter deviates up to 1 mag fainter than the VAMPIRES filters for later spectral types, the R filter has consistent colors compared to VAMPIRES except for the coolest stars, and the G filter can deviate up to 5 mag brighter compared to VAMPIRES, depending on the spectral type.

4.5. Absolute Flux Calibration

During commissioning, spectrophotometric standard stars HR 718 ($m_V = 4.273$) and HD 19445 ($m_V = 8.096$) were observed in each filter to calibrate the photometric zero points in Jy and e⁻ s⁻¹ (Hamuy et al. 1992, 1994; Stone 1996; Zacharias et al. 2013).

The absolute flux calibration is summarized by the C_{FD} coefficient, following Gordon et al. (2022). This flux density

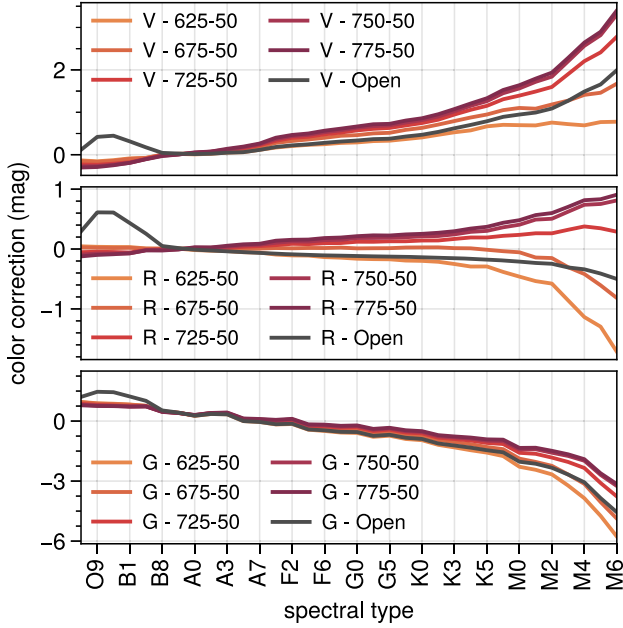


Figure 7. Color correction values for selected filters into the VAMPIRES bandpass filters. All correction values are tabulated from main-sequence Pickles stellar models. The spectral types are labeled on the x -axis. (Top) Johnson-Cousins V (Middle) Johnson-Cousins R (Bottom) Gaia G.

conversion factor converts between instrument flux (in $e^- s^{-1}$) and Jy. The instrument flux was measured using aperture photometry and corrected for atmospheric extinction using an empirical model from Buton et al. (2013). The conversion factors are derived from synthetic photometry of the calibrated stellar spectra.

The photometric zero points are mapped from Vega magnitudes to instrument flux in $e^- s^{-1}$ without a beamsplitter. The traditional zero point can be derived by incorporating each detector’s beamsplitter throughput and camera gain rather than specifying all 280 unique combinations.

The zero points are used by taking the aperture flux in $e^- s^{-1}$, corrected for any beamsplitter or FLC throughputs, and converting to magnitudes with the zero point magnitude:

$$m_{\text{filt}} = ZP_{\text{filt}} - 2.5 \log(f), \quad (7)$$

or, equivalently, with the zero point flux

$$m_{\text{filt}} = -2.5 \log(f/f_{ZP}). \quad (8)$$

The surface brightness, Σ_{filt} , can be calculated by dividing the calibrated flux by the area of a pixel ($\Omega_{\text{px}} = 3.5 \times 10^{-5} \text{ arcsec}^2 \text{ px}^{-1}$). For Vega magnitudes, instead, use

$$\Sigma_{\text{filt}} = m_{\text{filt}} + 2.5 \log(\Omega_{\text{px}}) = m_{\text{filt}} - 11.1 \text{ mag arcsec}^{-2}. \quad (9)$$

The accuracy of the zero points and conversion factors is constrained by atmospheric transmission variations along with dust accumulation and coating degradation of the telescope mirrors. Imaging a spectrophotometric standard at multiple

elevation angles for observations demanding the highest photometric precision will give better accuracy.

4.6. Limiting Magnitudes

Under excellent conditions, the detector integration time and saturation limit set the brighter end of the magnitude range. The fastest detector integration time is $7.2 \mu\text{s}$ in “fast” mode and 48 ms in “slow” mode (for the standard imaging mode with a $3'' \times 3''$ FOV). For these calculations, the peak count limit is set to 60,000 adu, and it is assumed that the brightest pixel in the PSF will be 30% the full aperture flux. The highest-throughput scenario (“Open” filter, no beamsplitter, no FLC; Table 5) translates the limiting instrumental flux into $m_{\text{Open}} = 2.1$ in “fast” mode and $m_{\text{Open}} = 11.7$ in “slow” mode. The AO WFS constrain the faint observing limits: the current guider limits of AO188 are $m_R < 16$, and the wavefront sensor limits for diffraction-limited imaging at visible wavelengths with SCEXAO are roughly $m_R < 10$ (Ahn et al. 2023).

The lunar phase primarily determines the sky background above Maunakea in the visible. The peak surface brightness is $\Sigma_R = 17.9 \text{ mag arcsec}^{-2}$ (Roth et al. 2016). Assuming, again, the highest-throughput observing configuration and using a pixel size of 5.9 mas, this corresponds to an instrument flux of $5 \times 10^{-2} e^- \text{ px}^{-1} \text{ s}^{-1}$. This is an order of magnitude higher than the dark signal (Table 2) and is the limiting noise term for exposures longer than 1.2 s.

5. The VAMPIRES Point-spread Function

One of the key parameters of a HCI instrument is the instrumental PSF and how close the on-sky performance reaches the ideal PSF. The observed VAMPIRES PSF quality varies depending on the residual wavefront error and the exposure time. Because the PSF fluctuates rapidly from residual atmospheric wavefront errors, integrating longer than the speckle coherence time ($\sim 4 \text{ ms}$, Kooten & Izett 2022) blurs the PSF. The speckled diffraction pattern can be “frozen” with fast exposure times, enabling lucky imaging. The high-speed detectors in VAMPIRES can easily take exposures faster than the coherence timescale, which makes it well-suited for this technique.

An annotated PSF in the F720 filter of HD 191195 after post-processing is shown in Figure 8. This data has a FWHM of 20 mas and a Strehl ratio²⁰ of $\sim 52\%$, which is typical performance for SCEXAO in average conditions (seeing of $0''.8$).

5.1. PSF Features

The PSF image in Figure 8 shows typical features of high S/N VAMPIRES observations. The center of the frame contains the

²⁰ The Strehl ratio is measured using a broadband synthetic PSF normalized to the photometric flux in a $0''.5$ radius aperture. The peak is subsampled with a Fourier transform, as in method seven (7) of Perrin & Marchis et al. (2004).

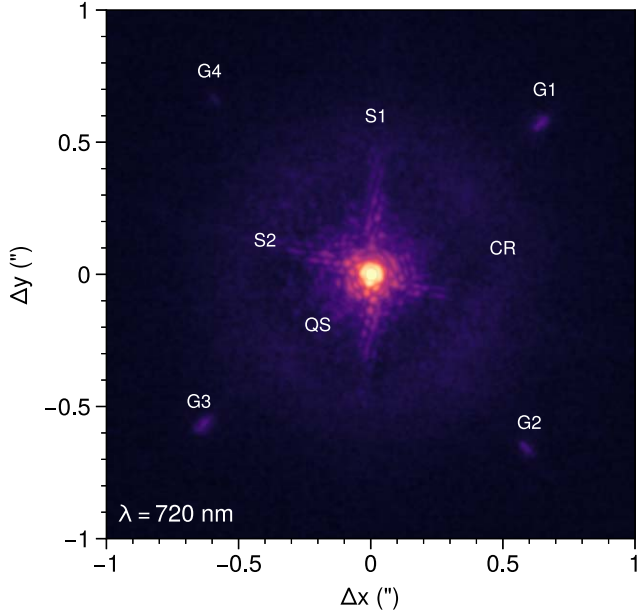


Figure 8. On-sky images of HD 191195 in the F720 filter (DIT = 2.3 ms). Data has been aligned and collapsed and is shown on a log scale with clipping to emphasize the fainter regions of the image. (G1–G4) passive speckles created by the diffractive gridding of the SCExAO deformable mirror. (S1–S2) Spider diffraction spikes. (CR) the SCExAO control radius, where a speckle halo creates an apparent dark hole. (QS) quasi-static speckles created by residual and non-common path wavefront errors.

central core and the first few Airy rings, which are slightly asymmetric due to wavefront errors. Beyond this are the quasi-static speckles (QS), which slowly evolve due to non-common path errors (Soummer et al. 2007; N’Diaye et al. 2013).

The PSF contains two large, bright diffraction spikes from the secondary mirror support structure (spiders; S1–S2). These spikes reduce image contrast if they align with a target in the field, but using coronagraphy (Section 6) or exploiting field rotation over time can mitigate the effects of these spikes.

The SCExAO DM has 45 actuators across the pupil, which limits the highest spatial frequency corrected by the AO loop to $\sim 22.5\lambda/D$. Typically, this is referred to as the control radius or “dark hole,” visible in the PSF image (CR). The dark hole is closer to a square in this image, determined by the modal basis used for wavefront sensing and control. The DM also acts like a diffractive element due to the gridding of the surface, which creates copies of the stellar PSF at four locations orthogonal to the orientation of the DM (G1–G4).

5.2. Seeing and the Low-wind Effect

The low-wind effect (LWE) is caused by piston wavefront discontinuities across the telescope pupil spiders (Milli et al. 2018). The effect in the focal plane is “splitting” of the PSF (Figure 9). Current WFS struggle to detect LWE, which periodically occurs in almost every VAMPIRES observation, although it can be

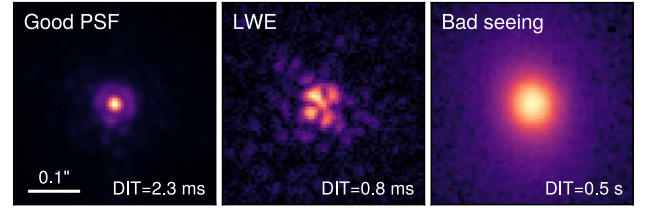


Figure 9. (Left) High-framerate image in good conditions shows a high-quality PSF (Strehl $\sim 52\%$). (Middle) high-framerate image highlighting LWE. (Right) a longer exposure image in poor seeing conditions is blurred into a Moffat-style profile. All images are shown with a square-root stretch with separate limits.

mitigated to an extent through frame selection. The other PSF image is of a fainter star ($m_R = 8.1$) with 0.5 s exposures. The PSF is fuzzy with a FWHM of 75 mas and low S/N resulting from the blurring of the residual speckle pattern throughout the integration.

5.3. Lucky Imaging

Figure 10 shows two observing scenarios: high framerate data (500 Hz) in median seeing conditions and low framerate data (2 Hz) in poor seeing conditions. A long exposure was simulated by taking the mean image; then, the data was registered using centroids. Progressively, from left to right, more frames are discarded based on the Strehl ratio, which shows that frame selection increases the PSF quality, but in poor conditions, it lowers the overall S/N for little gain.

5.4. Radial Profiles

The radial profiles of a high-quality PSF, a seeing-limited PSF, and a synthetic instrument PSF are shown in Figure 11. The ideal PSF is normalized to a peak value of 1 and the other profiles are normalized to the ideal PSF using a $1''$ aperture sum. The cumulative aperture sums, or encircled energy, are normalized to a value of 1 at $1''$ and shown alongside the radial profiles. The good, on-sky PSF closely matches the profile of the theoretical PSF until about $15\lambda/D$. The nulls of the radial pattern are not as deep as the model due to quasi-static speckles. Past $15\lambda/D$, the control radius of the SCExAO DM is clear due to the residual atmospheric speckle halo.

6. Coronagraphy

Coronagraphy is another key tool for HCI because it reduces the stellar diffraction pattern and attenuates the photon noise from the on-axis PSF. This is essential for observing faint objects near bright stars, such as exoplanets or circumstellar disks, by significantly reducing the glare from the star itself. Four visible-light Lyot-style coronagraphs were installed in VAMPIRES (Lucas et al. 2022). These coronagraphs provide up to three orders of magnitude of attenuation of the stellar PSF, which, when combined with extreme AO correction and low-noise detectors, enables contrasts $< 10^{-6}$ (Figure 11).

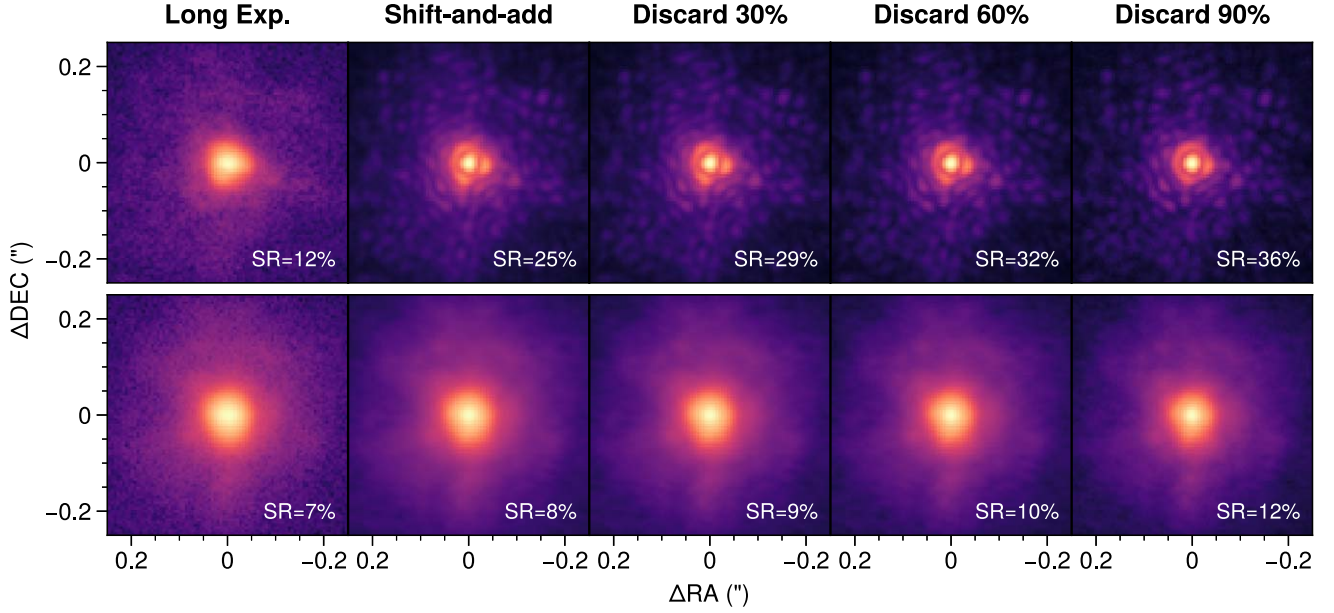


Figure 10. Post-processing data with lucky imaging. Each frame is shown with a log stretch and separate limits. (Top) high-framerate (500 Hz) data in median seeing conditions ($m_R = 4.3$). (Bottom) low-framerate (2 Hz) data in mediocre seeing conditions ($m_V = 9.2$). (Long Exp.) a mean combination without alignment, simulating a long exposure. (Shift-and-add) co-registering each frame before collapsing. (Discarding X%) same as shift-and-add but discarding a percentage of data based on the Strehl ratio.

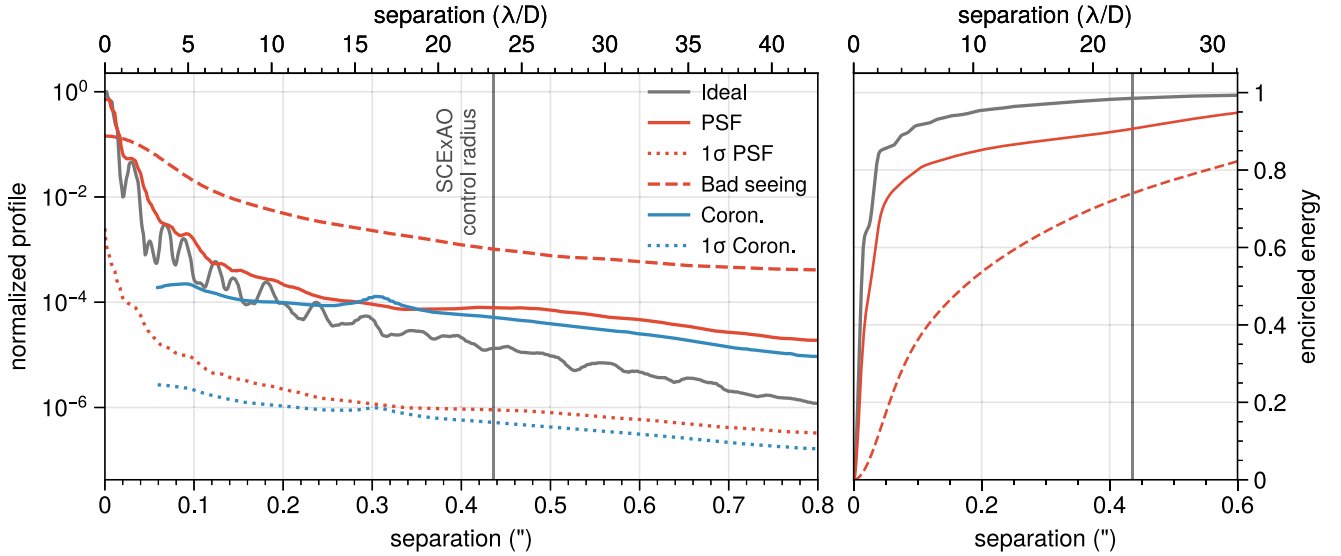


Figure 11. Radial profiles and encircled energy in different observing scenarios. (Left) radial profiles normalized to an ideal PSF (gray), a high-quality on-sky PSF (the same as Figure 8, solid red), a poor-quality on-sky PSF (the same as Figure 9, dashed red), and an on-sky coronagraphic PSF with the 59 mas IWA (solid blue). The 1σ raw contrast curves are shown for the good PSF (dotted red) and the coronagraphic PSF (dotted blue). The control radius of the SCEXAO DM is marked with a vertical gray line. (Right) the encircled energy normalized to an ideal PSF with a max radius of $1''$ (gray), a good on-sky PSF (solid red), and a poor-quality PSF (dashed red). The control radius of the SCEXAO DM is marked with a vertical gray line.

6.1. Focal Plane Masks

The four Lyot-style focal plane masks are partially transmissive (0.6%) circular dots with inner working angles (IWA) of two, three, five, and seven resolution elements (λ/D).

The focal plane masks are mounted in a three-axis translation stage for fine alignment. In addition, a double-grating vector vortex coronagraph (DGVVC; Doelman et al. 2023) was deployed in 2023 November. This mask is currently being evaluated.

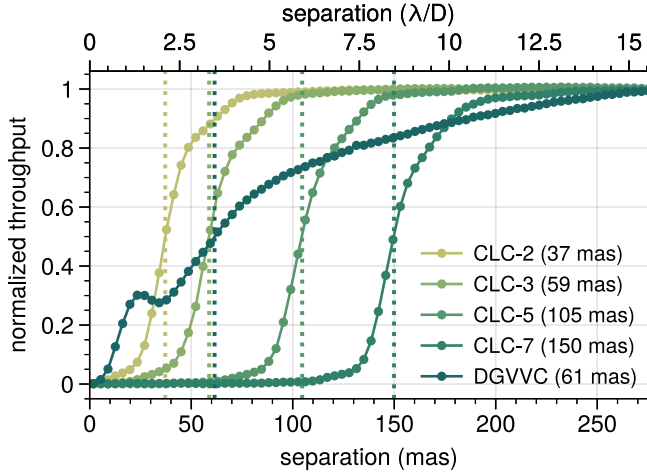


Figure 12. Normalized off-axis throughput for the VAMPIRES coronagraph masks. The throughputs are normalized to a range between 0 and 1. The inner working angle (IWA) is marked with vertical dotted lines at the point where the throughput reaches 50%. λ/D is determined from the average wavelength of the bandpass (680 nm).

The mask IWAs were measured by rastering the SCExAO internal calibration source across the focal plane mask and measuring the photometric throughput. The normalized throughput curves and IWA are shown in Figure 12, and the results are summarized in Table 7.

In practice, the CLC-2 mask is too small for on-sky observations—the residual tip-tilt in average conditions causes the PSF to leak out of the side of the mask. Due to the large size of the CLC-7 mask and because the Lyot stop was tuned to the CLC-3 and CLC-5 masks, the CLC-7 mask produces some diffraction that is not rejected by the Lyot stop. In poor observing conditions, this can create speckles that appear pinned to the edge of the mask. The CLC-3 mask is well-suited for good conditions (seeing $<0''.6$) or for polarimetric observations (thanks to the efficiency of PDI). The CLC-5 mask offers a good balance between robust diffraction control and IWA for all other scenarios.

6.2. Pupil Masks

VAMPIRES has three Lyot stop masks to reject the light diffracted by the coronagraphic focal plane mask. The first Lyot stop is described in Lucas et al. (2022). This mask is coated with gold for high reflectivity, aiding alignment with the pupil camera and for a future low-order wavefront sensor. Two new masks were designed with higher throughput and deployed in 2024 January (PI: Walk, A.). These masks were laser-cut from 1 mm thick aluminum foil sheets, which are not smooth or reflective enough to use with the pupil-viewing camera. Figure 13 shows all three Lyot stop masks imaged with a flat

Table 7
VAMPIRES Coronagraph Mask Specifications

Name	Radius (μm)	IWA (mas)
CLC-2	46	37
CLC-3	69	59
CLC-5	116	105
CLC-7	148	150
DGVVC	7	61

Note. The radius of the DGVVC is the radius of the central defect amplitude mask, which is resolved.

lamp alongside the VAMPIRES pupil. The mask specifications and throughput measurements are listed in Table 8.

6.3. Redundant Apodizing Pupil Mask

A redundant apodized pupil mask (RAP; Lebouilleux et al. 2022, 2024) was deployed on VAMPIRES in 2023 September. The mask shapes the pupil and was designed to create a deep 10^{-6} contrast dark zone in an annulus from 8 to $35\lambda/D$. The apodization pattern is resilient to up to ~ 1 rad of LWE, where the coherence of the PSF core starts to break down. The mask is designed with a trade-off between the size of the dark zone, the LWE resilience, and the mask’s overall throughput, which is $\sim 25\%$. The RAP mask, PSF, and radial profile are shown in Figure 14. Further testing and verification of this mask is future work.

6.4. Coronagraphic Point-spread Function

Figure 15 shows aligned and coadded on-sky coronagraphic PSFs for the CLC-3 and CLC-5 masks. The PSFs show some common features: a dark hole in the DM control region, calibration speckles, and a residual speckle halo slightly blurred from the coadding. The CLC-3 image shows a secondary diffraction ring past the edge of the mask. The control region in the CLC-5 image has worse contrast due to poorer atmospheric conditions that night. The radial profile for the CLC-3 mask is shown in blue alongside the non-coronagraphic PSFs in Figure 11.

6.5. Calibration Speckles

VAMPIRES uses the SCExAO DM to create calibration speckles (“astrogrid”) for precise astrometry and photometry of the star behind the coronagraph mask (Sahoo et al. 2020). The calibration speckles produce an “X” with theoretical separations of 10.3 , 15.5 , or $31.0\lambda/D$. The relative brightness of these speckles to the on-axis PSF allows for the precise photometry of coronagraphic images.

In the linear wavefront error regime (<1 rad), the brightness of a speckle is a quadratic function of the optical path

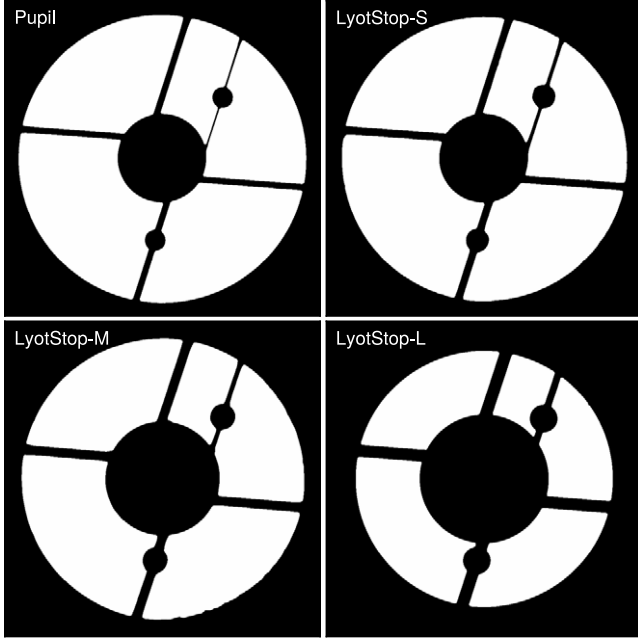


Figure 13. Images of the VAMPIRES pupil and coronagraphic pupil masks illuminated by a flat lamp. Images have been binarized to sharpen the edges. Each mask is labeled in the top left. The pupil image displays the SCEXAO pupil, which includes masks for broken deformable mirror actuators.

Table 8
Instrument Pupil and Lyot Stop Specifications

Name	D_{in} (mm)	D_{out} (mm)	T_{geom} (%)	T_{phot} (%)
Telescope Pupil	2300	7950
SCEXAO Pupil	5.27	17.92
VAMPIRES Pupil	2.08	7.06	100	100
LyotStop-S	2.14	7.06	95.9	89.2
LyotStop-M	2.82	6.99	85.7	79.7
LyotStop-L	3.16	6.33	61.5	57.2

Note. The telescope pupil is the effective pupil with the IR M2 (which undersizes the 8.2 m aperture).

difference (OPD; Jovanovic et al. 2015a; Currie et al. 2018; Chen et al. 2023) and, therefore, the ratio of the satellite spot flux to the central star (contrast) is

$$\frac{f_p}{f_*}(\lambda, A_{DM}) \propto (A_{DM}/\lambda)^2, \quad (10)$$

where A_{DM} is the mechanical displacement of the DM, λ is the wavelength of light.

The scaling coefficients for the most commonly used astrogrid patterns (10.3, 15.5, and $31\lambda/D$) were fit using multiband observations of the internal calibration source. When trying to fit Equation 10, a better agreement was found using a

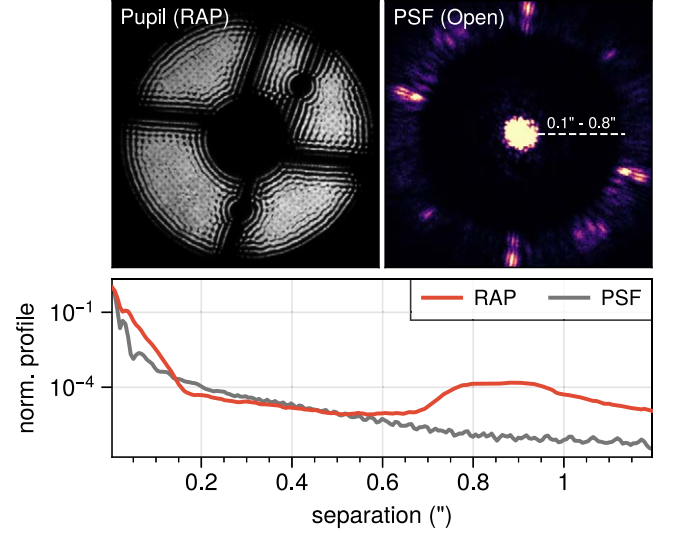


Figure 14. The redundant apodized pupil (RAP) mask. (Top left) a pupil image of the mask shows the apodization pattern. (Top right) a $2'' \times 2''$ FOV of the PSF produced by the RAP using the SCEXAO internal source in the Open filter. The image is stretched to emphasize the dark hole from approximately $0.1''$ to $0.8''$. (Bottom) a normalized radial profile of the top right PSF in log scale.

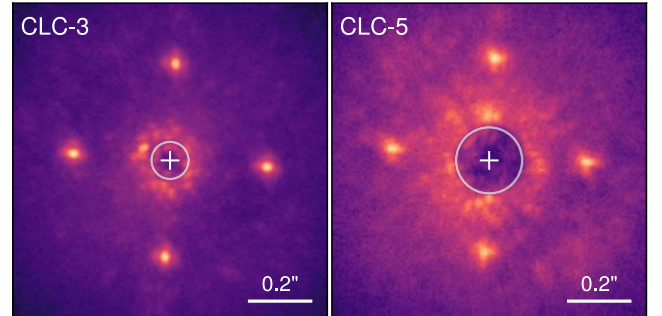


Figure 15. On-sky coronagraphic PSFs using the multiband imaging mode. (left) The CLC-3 mask from polarimetric observations of HD 163296. (right) the CLC-5 mask from polarimetric observations of HD 169142, which had slightly worse seeing conditions. Both are aligned and coadded from the F720 frame of single data cube, cropped to the inner $1''$ FOV, and shown with a logarithmic stretch and separate limits for each image. The calibration speckles are $\sim 15.5\lambda/D$ from the center. The coronagraph mask is overlaid with a white circle, and the approximate location of the star is marked with a cross.

model containing an additional linear OPD term—

$$\frac{f_p}{f_*}(\lambda, A_{DM}|c_0, c_1) = c_0 \cdot (A_{DM}/\lambda) + c_1 \cdot (A_{DM}/\lambda)^2, \quad (11)$$

which was fit using weighted linear least-squares, shown in Table 9 and Figure 16. The $31\lambda/D$ separation pattern has very low relative flux for the pattern amplitude due to the influence

Table 9
Astrogrid Relative Photometry Flux Scaling

Pattern	Separation (λ/D)	c_1	c_0
XYgrid	10.3	14.217 ± 1.489	-0.111 ± 0.093
XYgrid	15.5	7.634 ± 1.321	-0.043 ± 0.082
XYgrid	31.0	0.561 ± 0.256	-0.002 ± 0.023

Note. Photometry measured using elliptical apertures with local background subtraction. Astrogrid applied using 1 kHz modulation speed.

function of the DM, which has a weaker response for high spatial frequencies.

A trade-off exists between photometric and astrometric precision of the calibration speckles with increased contrast due to photon noise around them. The amplitude and separation of the astrogrid pattern should be tuned for optimal contrast over most of the control region. The wings of the PSF quickly fall below contrasts of $\sim 10^{-2}$ and the radial profile of the on-axis PSF is $\sim 10^{-4}$ where the calibration speckles land (Figure 11). If the speckle contrast is $< 10^{-2}$, then the astrogrid will not affect contrast outside of the speckle PSF cores. A relative brightness of 10^{-2} corresponds to an amplitude of 24 nm for the $10\lambda/D$ pattern, 28 nm for the $15.5\lambda/D$ pattern, and 103 nm for the $31\lambda/D$ pattern.

There are practical considerations for using astrogrid simultaneously with other SCEXAO modules. For example, when using SCEXAO/CHARIS for PDI, the field stop requires using the $10.3\lambda/D$ separation grid so that all the speckles land within the CHARIS FOV. The speckle brightness in the NIR is fainter, which means the optimal brightness for CHARIS data might produce brighter than optimal speckles in VAMPIRES. Lastly, for observations in the Open filter, the radial smearing of the satellite spots reduces the astrometric and photometric precision.

6.6. On-sky Contrast Curves

Contrast curves were measured for the CLC-3 and CLC-5 coronagraphs during commissioning. The CLC-3 contrast curve is discussed in Section 10.2. The CLC-5 contrast was measured from a 60 min sequence of HD 102438 ($m_R = 6.0$, Zacharias et al. 2017) with $\sim 10^\circ$ of field rotation. The conditions were good ($0''.45 \pm 0''.1$ seeing), but LWE caused frequent PSF splitting.

The data was post-processed with ADI.j1 (Lucas & Bottom 2020) using principal component analysis (PCA, or KLIP; Soummer et al. 2012) with 20 principal components for each multiband field. These results produce residual frames, which are then derotated and collapsed with a weighted mean (Bottom et al. 2017). The contrast was measured by dividing the noise in concentric annuli by the stellar flux, correcting for

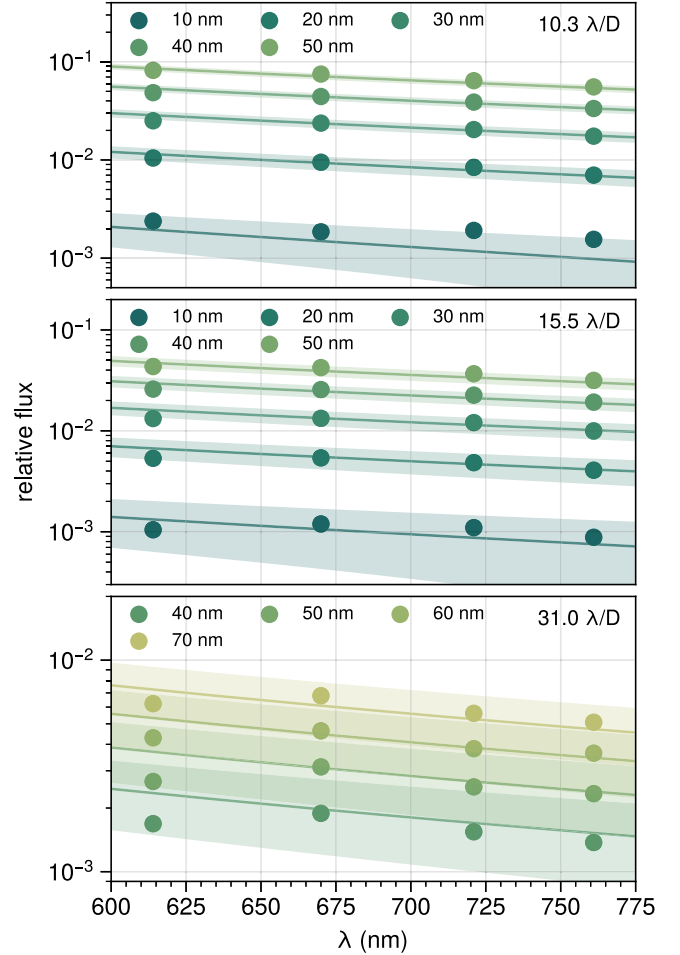


Figure 16. Relative photometric flux of the astrogrid calibration speckles. Each plot corresponds to a speckle pattern, and each curve corresponds to a given pattern amplitude (in mechanical microns applied to the DM). The best-fitting models with 1σ uncertainty bands are shown for each configuration.

small sample statistics (Mawet et al. 2014). Algorithmic throughput was measured by injecting off-axis sources and measuring the recovered flux after PSF subtraction. The contrast curves for each filter are shown in Figure 17.

The best contrast is achieved at the longest wavelengths, following the inverse wavelength scaling of optical path differences. There is a slight deviation from this behavior in the F760 filter at far separations where the curve becomes background-limited, which can be attributed to the lower average S/N in the truncated bandpass of the F760 filter (Table 5). Roughly 10^{-4} contrast was reached at the IWA ($0''.1$), 10^{-5} at $0''.4$, and 10^{-6} beyond $0''.6$.

6.7. Spectral Differential Imaging

The wavelength diversity of multiband imaging data was leveraged by performing SDI in two ways. The first was by

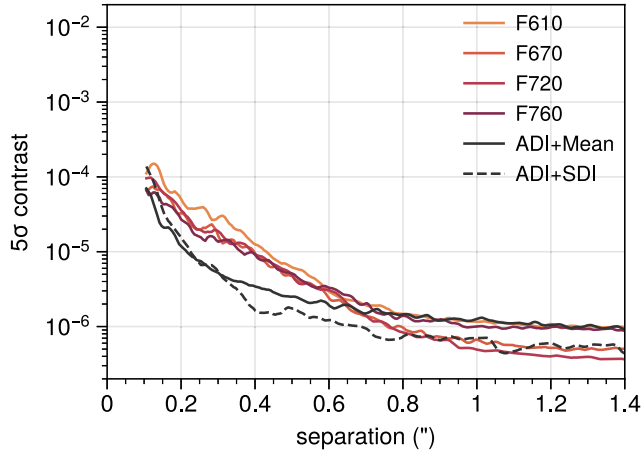


Figure 17. 5σ throughput-corrected Student-t contrast curves from multiband imaging of HD 102438 with the CLC-5 coronagraph. This was 60 minutes of data with 10° of field rotation. The contrast from the PCA (20 components) PSF subtraction for each MBI filter is shown with red curves. The solid black curve is the mean-combined residual contrast from each wavelength, and the dashed line is the median SDI-subtracted contrast curve.

taking each collapsed ADI residual frame and doing a mean combination of the residuals, attenuating uncorrelated noise (e.g., read noise). The second technique uses another round of PSF subtraction after radially scaling each frame by wavelength and multiplying by a flux factor (“ADI + SDI”). The median PSF from the scaled images was subtracted from the data before rescaling back to sky coordinates (“classical” SDI).

Fake companions were injected with the same spectrum as the star at equal contrasts for each wavelength for algorithmic throughput analysis. 5σ contrasts of 10^{-4} at were reached at the IWA ($0''.1$), 10^{-5} contrast at $0''.2$, and 10^{-6} beyond $0''.5$. In general, the SDI reduction achieves better contrast than individual ADI reductions alone, especially from $0''.1$ to $0''.7$.

6.8. Residual Atmospheric Dispersion

There is only one broadband ADC in the common path of SCEXAO (Egner et al. 2010), resulting in residual atmospheric dispersion at low elevations. This dispersion causes a differential shift of the PSF at each wavelength, which can be problematic for coronagraphy with multiband imaging because the PSF can leak outside the focal plane mask (Figure 18). With the CLC-3 mask, this effect is noticeable above an airmass of ~ 2.2 ($<27^\circ$ elevation). The larger masks (CLC-5 and CLC-7) are less affected by this leakage.

7. Imaging Polarimetry

Polarimetric differential imaging (PDI; Kuhn et al. 2001) is a powerful technique for high-contrast observations. By measuring orthogonal polarization states simultaneously through nearly the same optical path, the unpolarized signal in the

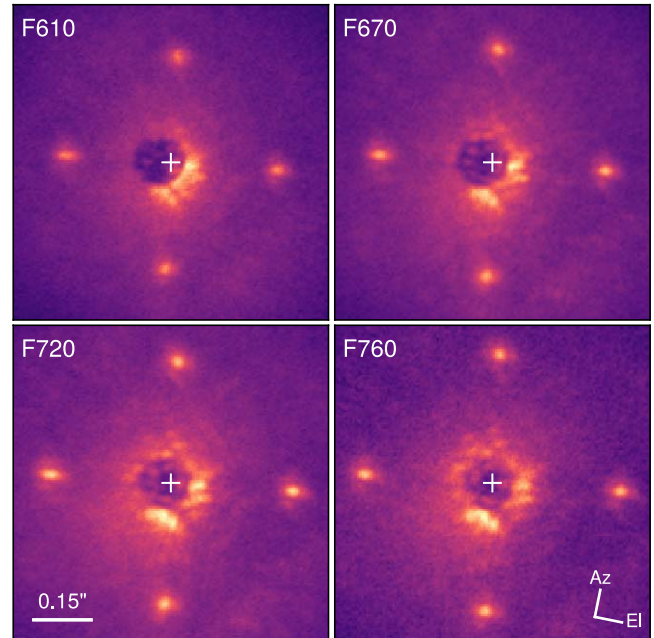


Figure 18. Coronagraphic multiband imaging with the CLC-3 coronagraph at 2.25 airmass (26.3° elevation). The filter is labeled at the top left, the apparent location of the star is marked with a cross, and the telescope elevation and azimuth axes are displayed with a compass at the bottom left. The image is shown with a square-root stretch with separate limits for each filter. The residual atmospheric dispersion differentially shifts the star in the focal plane, reducing the effectiveness of the coronagraphic diffraction control.

stellar PSF can be canceled to a high degree (less than $\Delta 10^{-4}$, Schmid et al. 2018). This differential approach significantly suppresses the stellar PSF, allowing the detection of faint polarized signals from circumstellar disks or exoplanets. Additionally, through polarimetric modulation, it is possible to remove or greatly reduce the effects of instrumental polarization and fast atmospheric seeing.

7.1. Polarimetric Differential Imaging

VAMPIRES is designed to measure linear polarization with high precision and accuracy. A polarizing beamsplitter cube splits horizontally polarized light (I_{0°) to VCAM1 and vertically polarized light (I_{90°) to VCAM2. This intensity mixes the inherently polarized signal and the inherently unpolarized signal (I_*)

$$I_{C1} = I_{0^\circ} + 0.5 \cdot I_*, \quad (12)$$

$$I_{C2} = I_{90^\circ} + 0.5 \cdot I_*. \quad (13)$$

Subtracting data from the two cameras yields the Stokes Q parameter, by definition—

$$I_{C1} - I_{C2} = I_{0^\circ} - I_{90^\circ} + 0.5 \cdot (I_* - I_*) = Q. \quad (14)$$

Conveniently, the unpolarized stellar signal is completely removed by this subtraction.

To measure Stokes U , which is the difference of light at 45° and 135° —

$$U = I_{45^\circ} - I_{135^\circ}. \quad (15)$$

The input signal is modulated with a HWP so that I_{45° and I_{135° are retarded into horizontally and vertically polarized light, which then can be measured by the cameras.

In theory, the subtraction in the definition of the Stokes observables removes the unpolarized signal, but, in reality, the imperfections of the polarimeter leave instrumental polarization and non-common path errors (Kuhn et al. 2001; Tinbergen 2005). Every inclined reflective surface will partially polarize otherwise unpolarized light, and these reflections are difficult to avoid in a complicated instrument like SCEXAO mounted on a Nasmyth platform (Tinbergen 2007). The instrumental polarization is a nuisance term in the analysis, but a majority of it is canceled by the HWP modulation—rotating the HWP 45° switches the sign of the observable (Stokes Q becomes $-Q$). The difference ($[Q - (-Q)]/2$) removes the instrumental polarization downstream of the HWP.

7.2. High-speed Polarimetric Modulation

Switching orthogonal polarization states at the same rate or faster than the atmospheric speckle timescale (\sim ms) differentially removes these fast speckles with high precision during the polarimetric data reduction (Kemp 1969). This fast modulation technique has been successfully implemented on several aperture polarimeters (Rodenhuis et al. 2012; Harrington et al. 2014; Bailey et al. 2015, 2017, 2020), seeing-limited polarimeters (Safonov et al. 2017; Bailey et al. 2023), and high-contrast polarimeters (Norris et al. 2015; Schmid et al. 2018).

VAMPIRES uses a FLC for fast polarimetric modulation. The FLC behaves like a HWP whose fast-axis rotates 45° when a voltage is applied. VAMPIRES was upgraded with an achromatic FLC rotator,²¹ which has better retardance across the bandpass than the previous one. The initial characterization of the FLC shows a $\sim 20\%$ improvement in the efficiency of measuring the linear Stokes parameters.

The FLC switches in less than $100 \mu\text{s}$, which is synchronized with every detector exposure (1 Hz to >1 kHz). The new FLC is mounted in a temperature-controlled optical tube at 45°C for consistent, efficient modulation and to avoid any temperature-dependent birefringence of the liquid crystal. The FLC photometric throughput is 96.8%. The FLC has a maximum excitation time of 1 s, which means it can only be used with short exposures. The FLC mount was motorized to allow removing it for “slow” polarimetry, which only uses the HWP for modulation.

²¹ Meadowlark FPA-200–700.

7.3. Instrumental Modeling and Correction

Polarimetric measurements are limited by instrumental polarization due to the many inclined surfaces and reflections in the common path of VAMPIRES, in particular from M3 (Tinbergen 2007). Mueller calculus is a well-established technique to model and remove the instrumental effects (Perrin et al. 2015; Holstein et al. 2020; Joost’t Hart et al. 2021). The Stokes parameters measured through difference imaging are a measurement of the input Stokes values modified by the telescope and instrument Mueller matrix—

$$S(x, y) = \mathbf{M} \cdot S_{\text{in}}(x, y), \quad (16)$$

where S represents Stokes vector at each point in the field. With a calibrated model of \mathbf{M} , the instrument Mueller-matrix, Equation (16) can be solved using a least-squares fit to estimate the input Stokes vector (Perrin et al. 2015).

For VAMPIRES the Mueller matrix, \mathbf{M} , is estimated with a forward model. This model includes offset angles, diattenuations, and retardances for the polarizing components in each filter (Zhang et al. 2023). The model is fit to calibration data with a polarized flat source—these calibrations are automated for consistent monitoring of the instrument’s polarimetric performance.

The telescope tertiary mirror is a significant source of instrument polarization due to the small focal ratio (F/13.9) and 45° inclination (Schmid et al. 2018; van Holstein et al. 2023). Because the internal polarized source is after M3 (Figure 1), these birefringent effects cannot be easily calibrated without on-sky observations. A full instrument characterization and measurements of unpolarized ($p < 0.01\%$) and polarized ($p > 1\%$) standard stars to calibrate the effects of M3 is future work (Zhang et al. 2023). Observers needing high-precision polarimetry should observe an unpolarized and a polarized standard star: at least one HWP cycle at the beginning and end of the science sequence.

8. Polarimetric Differential Interferometry

VAMPIRES features a single telescope interferometric mode through non-redundant aperture masking (NRM). NRM is implemented by placing an opaque mask with a sparse array of sub-apertures in the pupil plane of the instrument. Four masks are available for use with VAMPIRES (Figure 19).

The non-redundant spacing of these sub-apertures, wherein each has a unique vector separation, ensures unique measurements of each baseline length (Fourier component) of the astrophysical scene (Tuthill et al. 2000). Unambiguous measurements of each Fourier component yield observables that are robust to atmospheric seeing and, as such, do not contain “redundancy” noise that grows with the square root of the number of measurements. As a result, NRM allows for the reconstruction of information at angular resolutions at and beyond the diffraction limit (Labeyrie et al. 2014). Combining

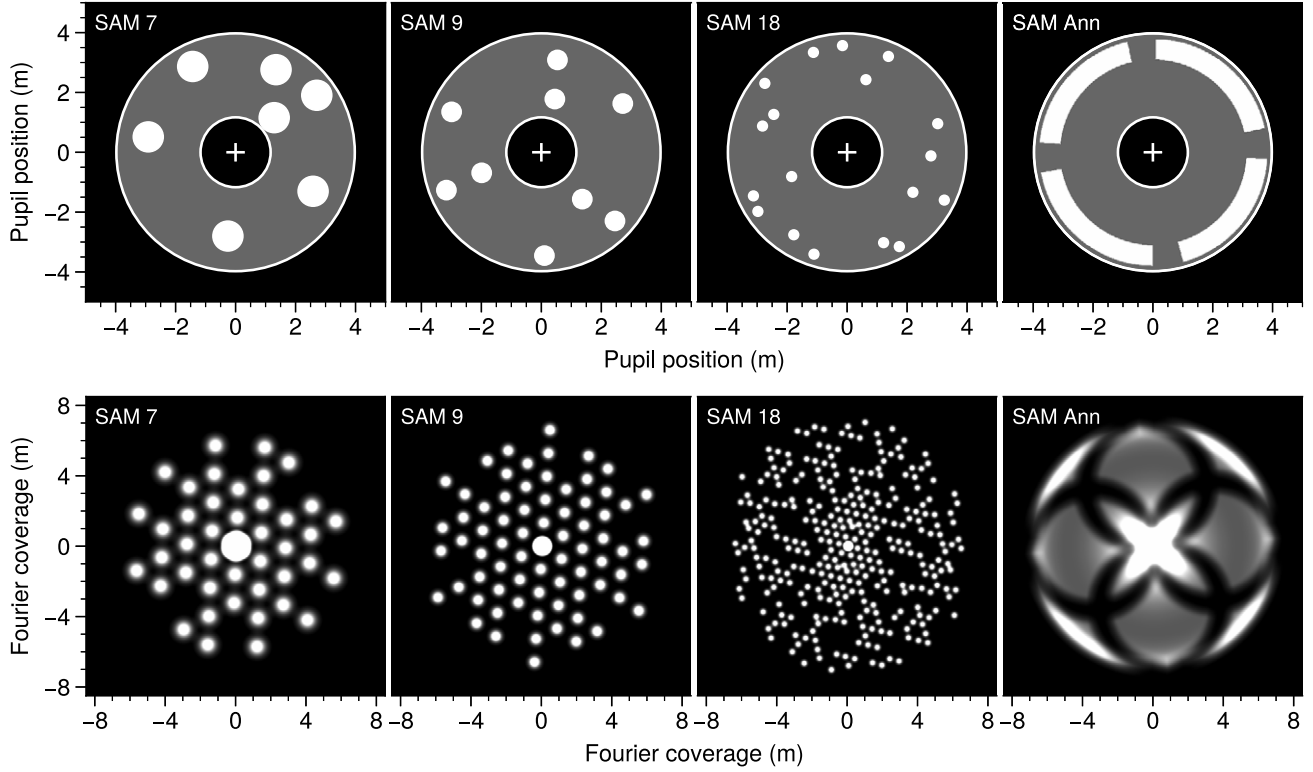


Figure 19. The four aperture masks available for use with the VAMPIRES instrument. (Top) design of masks in the pupil plane. The masks are named according to the number of sub-apertures. (Bottom) u, v -plane Fourier coverage. The choice of the mask is a function of the required Fourier coverage and the required throughput for a high signal-to-noise measurement of a target.

the advantages of NRM with those of polarimetry (Sections 2, 7) enables sub-diffraction limited measurement of polarized signal within the previously inaccessible regions of the image. In particular, the NRM mode unlocks regions obscured within the coronagraphic masks’ inner-working angle (Section 6). In this way, the NRM and coronagraphic modes operate in a complementary fashion—the outer working angle of the NRM mode is approximately the inner working angle of the coronagraph (Norris et al. 2015), and together, these modes provide near complete coverage of the circumstellar environment, right down to the stellar surface. For an appropriate choice of target (notably, bright enough to counteract the throughput loss of the mask), the NRM mode of VAMPIRES provides a powerful characterization of polarized circumstellar environments, limited only by contrast.

The interferometric observables are the differential, polarimetric analogs of standard visibilities and closure phases. They are self-calibrated (no calibrator star is required, and errors induced by AO are removed) and relatively immune to non-common path instrumental noise (Norris et al. 2015). Raw data is reduced to visibilities and closure phases using the VAMPIRES branch of the AMICAL package (Soullain et al. 2020) and further reduced to differential visibilities and closure

phases using a custom-tailored pipeline (Lilley et al. 2024, in preparation). An example of these observables is shown in Figure 20. Models and images of the astrophysical scene can then be fit to these resulting observables. Techniques for model fitting and novel machine learning-based image reconstruction techniques are currently in development. They will be released soon, along with early science results obtained using the NRM mode (Lilley et al. 2024, in preparation).

The VAMPIRES upgrades provide several key improvements for NRM. First, the MBI (Section 2.4) mode enables simultaneous measurement of differential observables (e.g., spectral differential phase), allowing for the high-precision characterization of circumstellar dust grain size and species. This improves observing efficiency by a factor of four, compared to repeating observations for different filters. Since the time-varying wavefront error is simultaneously sampled across wavelengths, direct interferometric phase measurements between spectral components can be produced. The increased observing efficiency enables the observer to accumulate more parallactic angle coverage, which is critical for characterizing non-azimuthal scattering symmetries. The new qCMOS detectors have a higher dynamic range and faster framerate than the previous EMCCDs Section 3, which creates sharper

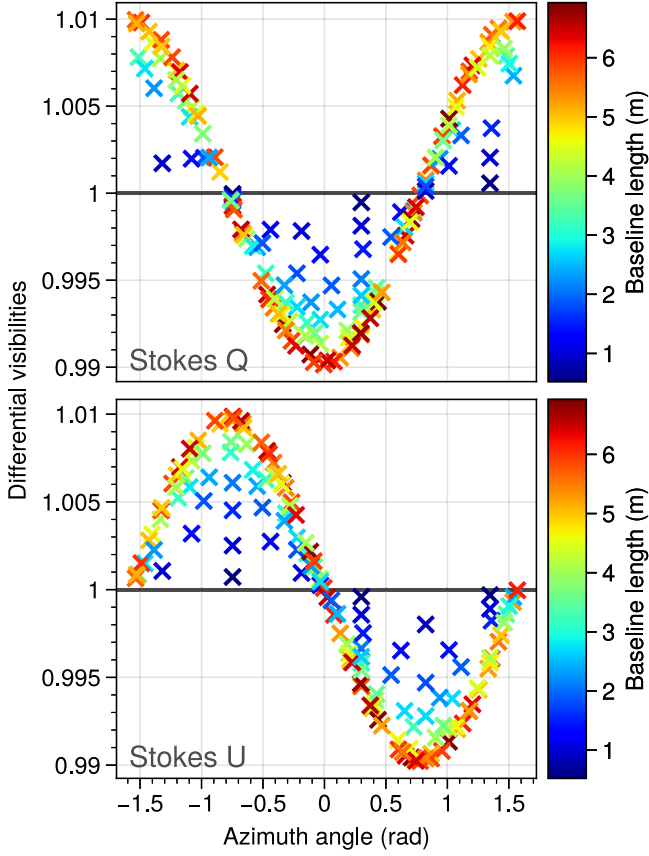


Figure 20. Polarimetric, differential visibilities for a model of a spherically symmetric circumstellar shell. Visibilities for a symmetric source have a distinctive sinusoidal appearance. Differential visibilities are produced for Stokes Q (top) and Stokes U (bottom), which describe the complete characterization of the linearly polarized circumstellar environment.

fringes without saturation for sufficiently bright targets. The qCMOS detectors also have better sensitivity in the photon-starved regime, as they do not suffer from the excess noise of electron multiplication from which EMCCDs suffer (Figure 4). The development and characterization of the NRM mode are ongoing, and a comprehensive analysis will be published in the near future (Lilley et al. 2024, in preparation).

9. Data Processing

A purpose-built open-source data processing pipeline for VAMPIRES is under development.²² This pipeline is designed to reduce data for both versions of the instrument and focuses on frame calibration, alignment, and polarimetry. The pipeline works for all observing modes, except non-redundant masking, and produces calibrated and coadded data ready for post-processing with other tools.

²² https://github.com/scexao-org/vampires_dpp

9.1. Pre-processing

For pre-processing the data is organized by type and object. Master calibration files are prepared from dark frames, sky frames, and flat frames. Multiband flats require an additional step to fit and normalize each multiband field independently. The final pre-processing step prompts the user to click on the approximate center of the field of view to aid in registration.

9.2. Frame Calibration and Collapsing

Raw data is calibrated with dark subtraction, flat-field normalization, and bad-pixel correction. Data is converted into units of $e^- s^{-1}$ and the FITS headers are normalized across the different instrument versions. Precise proper motion-corrected coordinates and parallactic angles are calculated from GAIA astrometry, when available (Gaia Collaboration et al. 2016, 2018, 2021).

After calibration, the frame centroid is measured using cross-correlation with a PSF model—for coronagraphic data, the four satellite spots (Section 6.5) are measured independently. The data is registered with the centroids and PSF statistics like the Strehl ratio, FWHM, and the photometric flux are measured. The individual FOVs in multiband data are analyzed separately and then cut out and stacked into a spectral cube. Absolute flux calibration is supported by providing a stellar spectrum, either a model or a calibrated spectrum, which is used for synthetic photometry to derive the flux conversion factor.

The data is collapsed with optional frame selection for lucky imaging. The registered and collapsed data frames are saved to disk for post-processing with other tools, such as `ADI.jl` (Lucas & Bottom 2020), `VIP` (Gomez Gonzalez et al. 2017; Christiaens et al. 2023), or `PyKLIP` (Wang et al. 2015).

9.3. Polarimetry

Polarimetric data is collated into sets for each HWP cycle and Stokes cubes are produced from the double- or triple-difference procedure. Before differencing, data are corrected for small differences in plate scale and angle offset between the cameras. The Stokes cube is optionally corrected with a Mueller-matrix, following Holstein et al. (2020), Zhang et al. (2023). Finally, all the individual Stokes cubes are derotated and median-combined. The Stokes I , Q , and U frames are saved alongside the azimuthal Stokes parameters Q_ϕ and U_ϕ (Monnier et al. 2019; Boer et al. 2020)–

$$\begin{aligned} Q_\phi &= -Q \cos(2\phi) - U \sin(2\phi) \\ U_\phi &= Q \sin(2\phi) - U \cos(2\phi), \end{aligned} \quad (17)$$

where

$$\phi = \arctan\left(\frac{x_0 - x}{y - y_0}\right) + \phi_0 \quad (18)$$

in image coordinates. Note, this is equivalent to the angle east of north when data has been derotated. The total linear

polarization,

$$P = \sqrt{Q^2 + U^2}, \quad (19)$$

and the angle of linear polarization,

$$\chi = \frac{1}{2} \arctan \frac{U}{Q}, \quad (20)$$

are also calculated and saved in the output cube.

10. Commissioning Results

The VAMPIRES upgrades were tested on-sky from 2023 June to August. Some results from the commissioning observations are presented below. During testing, many of the instrument configurations (polarimetry, coronagraphy, multiband imaging, narrowband imaging) were explored to verify that VAMPIRES is ready for observers. All data were obtained using the 188-mode correction from AO188 and ~ 1100 corrected modes, on average, with SCEXAO.

10.1. Spectro-polarimetric Imaging of HD 169142

VAMPIRES spectro-polarimetric capabilities are highlighted with multiband imaging of the young star HD 169142. This system hosts a protoplanetary disk (Quanz et al. 2013) and emission signatures from potential protoplanets (Hammond et al. 2023). The disk itself is nearly face-on ($i \sim 13^\circ$), and includes two rings ($R_{\text{in}} \sim 170$ mas, $R_{\text{out}} \sim 720$ mas), with a gap between them. A cavity is close to the star within the inner ring (Fedele et al. 2017).

This system has been imaged in polarized light by Kuhn et al. (2001), Quanz et al. (2013), Monnier et al. (2017), Pohl et al. (2017), including in the visible with ZIMPOL by Bertrang et al. (2018). The polarized images match the radio continuum disk morphology, comprising a bright inner ring with a fainter outer ring. The disk is nearly face-on, with an estimated inclination close to 13° (Fedele et al. 2017).

HD 169142 was observed with VAMPIRES in the “slow” polarimetry mode (no FLC) with the 105 mas Lyot coronagraph for 55 minutes, resulting in 47 minutes of data—roughly an 85% observing efficiency, including all overheads from external triggering and HWP rotation. The average seeing for the night from the Maunakea Weather Center (MKWC) archive²³ was 0.8 ± 0.2 .

The data was reduced as described in Section 9 with background subtraction and double-difference polarimetric reduction. Mueller matrices were adapted from Zhang et al. (2023) for the common-path HWP, image rotator, and generic optics term (i.e., excluding the detector intensity ratio and the FLC, since these components were modified in the upgrade). Residual instrumental polarization was corrected using the photometric sums in an annulus from $0.24''$ to $0.33''$, which matches the cavity of the disk (Bertrang et al. 2018).

The Stokes Q_ϕ frames, which are approximately equal to the polarized intensity, are shown in Figure 21. The inner disk is evident, with some diminished intensity to the southwest. A version scaled by the squared stellocentric distance to normalize the stellar irradiation is also shown, highlighting the disk gap and the inner rim of the outer disk.

Radial profiles with bin sizes of 4 pixels from each Q_ϕ frame and each Stokes I frame were measured from the coronagraph IWA ($0.1''$ out to $1.4''$). The ratio of these profiles is shown alongside the Q_ϕ profiles in Figure 22. The mean integrated partial-polarization of the disk is 0.6% across all wavelengths and the scattering intensity is higher at redder wavelengths.

Future work includes modeling geometric disk profiles to analyze the scattering geometry of this disk, allowing a measurement of the scattering phase function of the dust at multiple wavelengths. These measurements give color information about the scattering properties of the dust, which generally requires multiple observations for each filter or integral-field spectroscopy, but with VAMPIRES, they are obtained in one observing sequence using multiband imaging.

10.2. Imaging of HD 1160B

HD 1160 is an A0V star with two substellar companions (Nielsen et al. 2012; Maire et al. 2016; Garcia et al. 2017; Mesa et al. 2020). The inner companion, HD 1160B, is an M5–M7 brown dwarf with $0.7''$ separation on a 252–1627 yr orbit (Blunt et al. 2017). HD 1160 was observed on 2023 July 11 using VAMPIRES multiband imaging with a 59 mas IWA coronagraph for a relatively short sequence (17 minutes, 14° PA rotation). The data was processed with light frame selection (discarded the worst 25% of frames) and flux calibrated using an A0V stellar model. HD 1160B was not detected in the calibrated frames, alone.

PSF subtraction was performed at each wavelength using an iterative ADI algorithm (GreeDS; Pairet et al. 2019, 2020; Stapper & Ginski 2022). The companion was easily detected using 20 principal components. The ADI residuals were combined with and without SDI (Section 6.7). The residual frames are shown in Figure 23. The throughput-corrected contrast curves (Figure 24) were measured following the same procedure as Section 6, except with a mask for the companion to avoid bias.

To determine the precise astrometry of the companion, KLIP-FM (Wang et al. 2015) was used to forward model a synthetic PSF processed by the KLIP algorithm (Pueyo 2016). For this modeling, 50 principal components were used for each wavelength before mean-collapsing along the spectral axis. The forward-modeled PSF was used to perform an MCMC fit for the position of the companion in the residual frame. The 95% highest posterior density for the separation was 798.6 ± 1.9 mas at a position angle of $(247.07 \pm 0.15)^\circ$. This measurement was used for the astrometric calibration in Section 3.

²³ <http://mkwc.ifa.hawaii.edu/current/seeing/index.cgi>

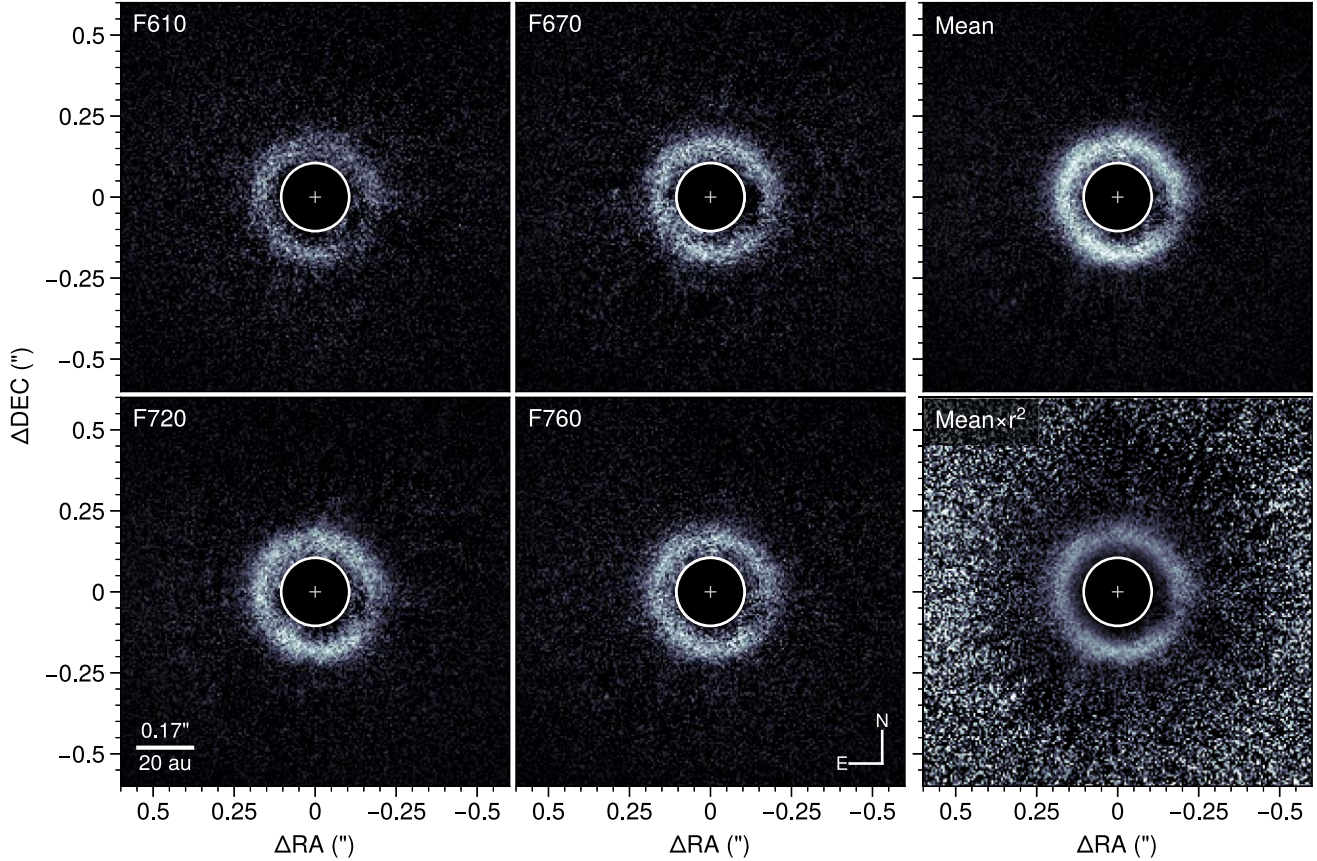


Figure 21. VAMPIRES polarimetric observations of HD 169142 in multiband imaging mode. The Stokes Q_ϕ frames are cropped to the inner $1''.2$ FOV with the coronagraph mask marked with a black circle. The data from each multiband filter is shown in the left four quadrants, and the wavelength-collapsed data is shown in the right column. The bottom-right image is multiplied by the squared stellocentric distance (r^2), which better shows the edge of the ring at $\sim 0''.4$. All data are rotated north up and east left and shown in a linear scale with separate limits for all images.

10.3. Narrowband Imaging of the R Aqr Nebula

VAMPIRES high angular resolution, dynamic range, and sensitivity are highlighted by emission line imaging of the innermost regions of the jets and binary of R Aqr. R Aqr is a symbiotic binary—the primary component is an AGB star (a Mira variable) and the secondary is a white dwarf (WD; Merrill 1935, 1940). Due to the proximity of the WD (10–50 mas over the orbit), matter is transferred directly from the giant star onto a compact accretion disk around the WD, creating a bipolar jet that extends $\sim 30''$ to the NE and SW (Schmid et al. 2017, and references therein). The 42 yr orbit of the binary has been studied in detail using radial velocity measurements, and recently with visual ephemerides from visible and radio imaging (Gromadzki & Mikołajewska 2009; Bujarrabal et al. 2018; Alcolea et al. 2023).

The WD companion has not been detected directly in the visible/NIR; at radio wavelengths, the CO continuum can be mapped with sufficient angular resolution to resolve the WD (Bujarrabal et al. 2018; Alcolea et al. 2023). Schmid et al. (2017)

showed using ZIMPOL that there is a bright $H\alpha$ emission feature coincident with the WD, thought to be a compact accretion disk and the origin of the bipolar jet. In 2020, a periastron passage occurred, putting the WD only a few au from the AGB star. This periastron passage was studied at many wavelengths (Hinkle et al. 2022; Sacchi et al. 2024).

R Aqr was observed with VAMPIRES on 2023 July 7 using the narrowband $H\alpha/H\alpha$ -continuum filter pair. Relatively long exposures were used (1.2 s), which blurred the PSF and reduced the efficacy of lucky imaging (Figure 10). The seeing during the observation was $0''.8 \pm 0''.2$ from the MKWC DIMM data, and the FWHM in the continuum image was 32 mas with a Strehl ratio of 15%. The collapsed $H\alpha$ image is shown in Figure 25, and a side-by-side of the inner region with the continuum is shown in Figure 26.

The data shows a resolved PSF-like clump to the northeast and diffuse emission extending from NE to SW. A separation of 50.0 mas at a position angle of 65° east of north was measured using PSF models.

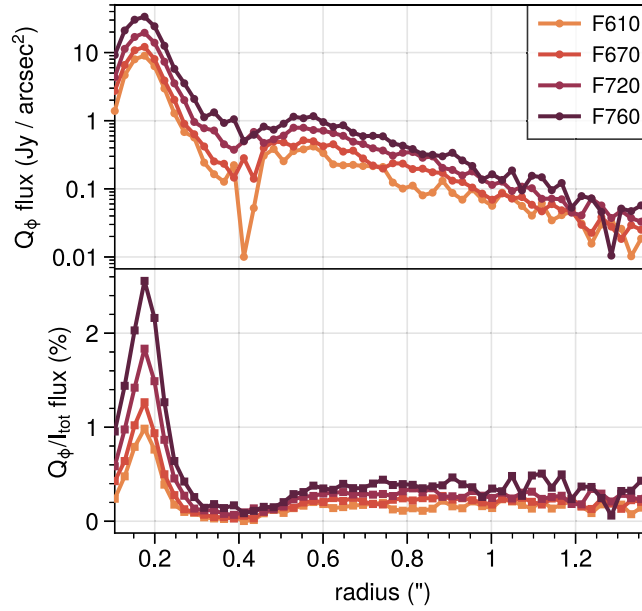


Figure 22. Radial profiles from multiband polarimetric images of HD 169142 for the polarized intensity (top; taken from Q_ϕ frame) and fractional polarized flux (bottom; Q_ϕ/I). The profiles are taken with annuli of a width of 4 pixels starting from the coronagraph IWA (105 mas). The region of the inner disk shows clearly that there is more dust scattering at redder wavelengths.

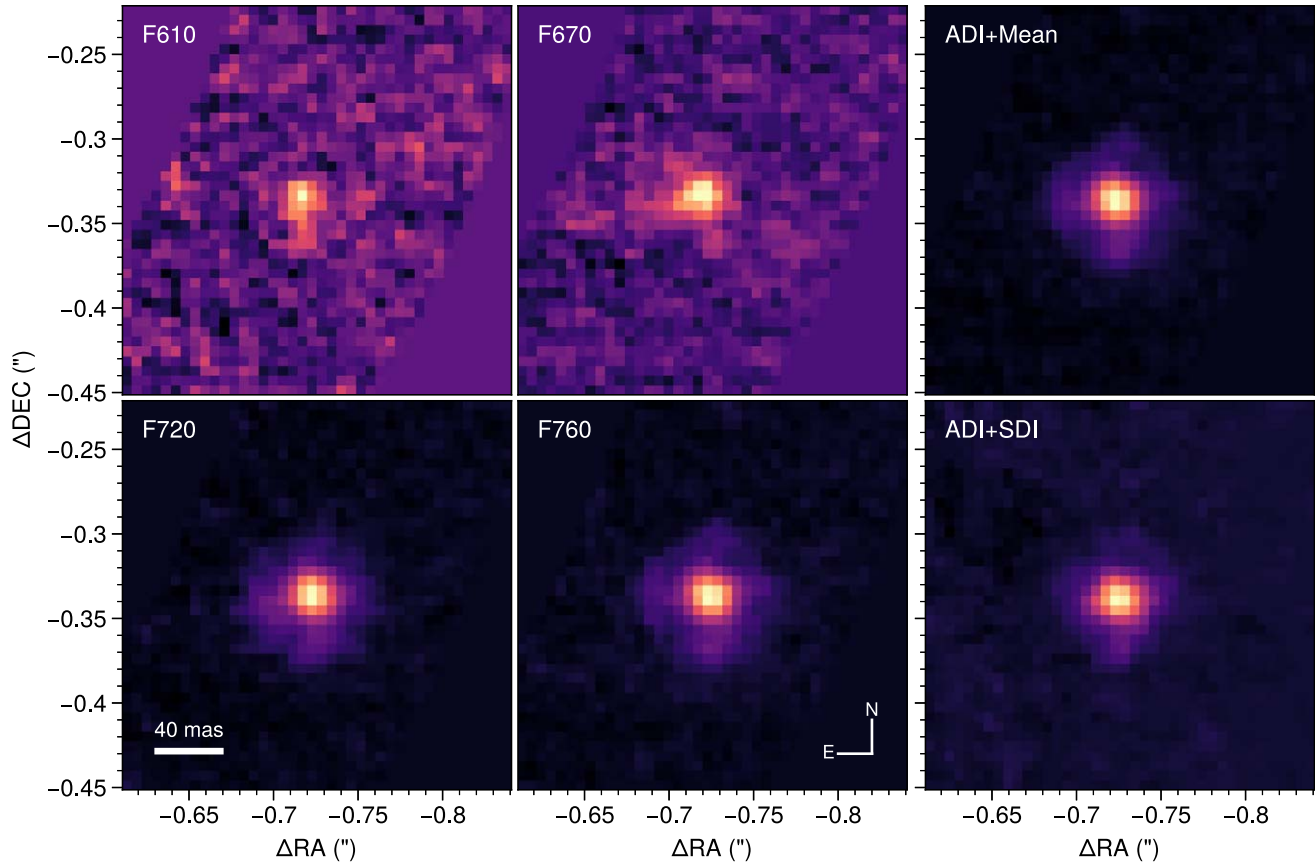


Figure 23. ADI residual frames from VAMPIRES observations of HD 1160 zoomed into a 40 px-crop around the companion HD 1160B. Data are shown with a linear scale and different limits for each frame. All frames were processed using the GreeDS algorithm with 20 principal components. The left four frames are residuals from each multiband filter. The top-right frame is the wavelength-collapsed residual, and the bottom-right frame is the ADI+SDI residual which includes a median PSF subtraction in the spectral domain. The ADI+SDI residual has a radial subtraction signature pointing towards the host star due to SDI PSF subtraction.

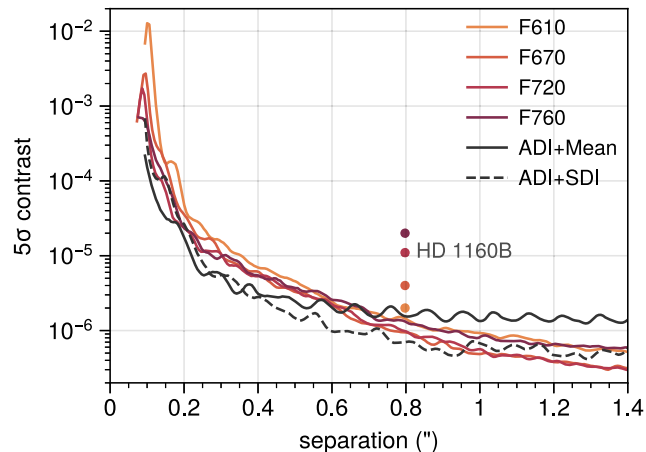


Figure 24. 5σ throughput-corrected Student-t contrast curves from multiband imaging of HD 1160 with the CLC-3 coronagraph. This was 16 minutes of data with $14^\circ 4$ of field rotation. The contrast from the GreeDS (20 components) PSF subtraction for each MBI filter is shown with red curves. The solid black curve is the mean-combined residual contrast from each wavelength, and the dashed line is the median SDI-subtracted contrast curve. The contrast of HD 1160B at each wavelength is shown with points.

Interestingly, this does not match the observations of Bujarrabal et al. (2018), Alcolea et al. (2023) (Figure 26), the $H\alpha$ emission clump is no longer co-located with the WD companion. Unpublished high-resolution ALMA CO observations from a month after these observations show that the WD now has an asymmetric jet following its periastron passage (J. Alcolea 2024, private communication). The location of the asymmetric jet is consistent with the observed $H\alpha$ emission north of the actual position of the WD. Future $H\alpha$ observations tracking the evolution of the jet emission are planned and will provide insight into the dynamical evolution of the R Aqr system.

10.4. Spectro-polarimetric Imaging of Neptune

Neptune is a compelling target for polarimetric imaging due to its dynamic gaseous atmosphere, which presents a unique opportunity to study scattering processes distinct from those in circumstellar disks (where single-scattering events dominate). Neptune has previously been imaged with ZIMPOL (Schmid et al. 2006) when it was installed on the ESO 3.6 m telescope.

In this work, we present high-resolution spectro-polarimetric observations of Neptune with VAMPIRES, taken on 2023 July 11 in slow polarimetry mode. The angular diameter of Neptune ($2''.3$) sat comfortably within the VAMPIRES FOV, eliminating the need for dithering. The AO performance was hindered due to the lack of a clear point source to use as a natural guide star. The planetary ephemeris from JPL horizons²⁴ is shown in Table 10.

²⁴ <https://ssd.jpl.nasa.gov/horizons/>

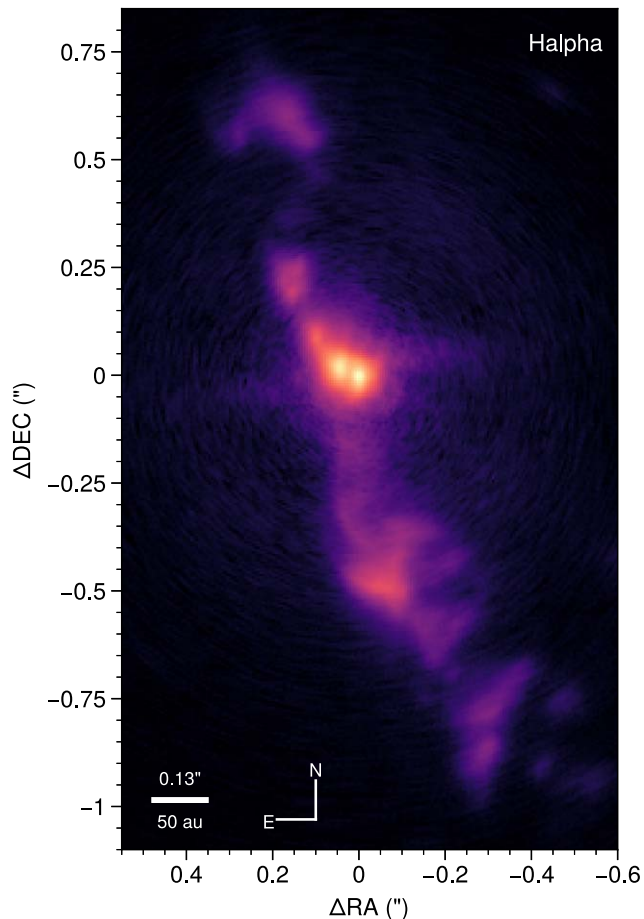


Figure 25. VAMPIRES $H\alpha$ narrowband image of R Aqr with logarithmic stretch showing the emission nebula. A faint diffraction spike, which is not astrophysical, can be seen roughly aligned with the R.A. axis around the central source.

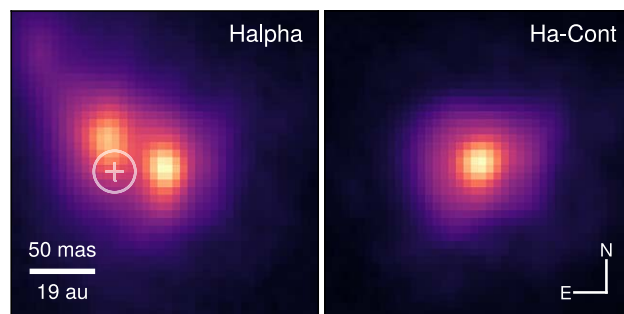


Figure 26. A zoom-in of the inner $0''.24$ FOV of R Aqr. (left) $H\alpha$ narrowband image shows the AGB star and a bright jet emanating from the WD. The expected location of the WD from the orbit of Alcolea et al. (2023) is marked with a white circle one FWHM in width. (right) $H\alpha$ -continuum image, which only contains emission from the AGB star.

For processing, each frame was registered using a cross-correlation with the average image. Calibration factors from Table 5 were used for absolute flux calibration. Similar to Section 10.1, the polarimetric reduction used double-

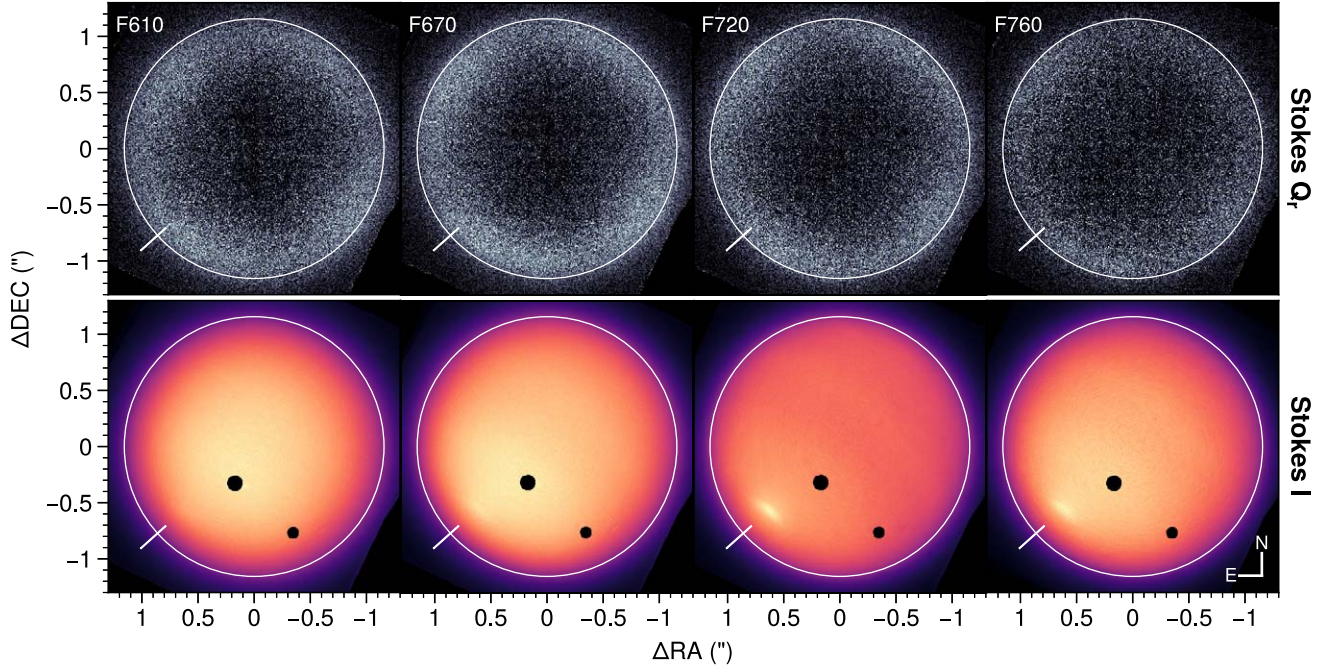


Figure 27. Multiband VAMPIRES observations of Neptune. All data are rotated so to north up and east left in linear scale with different limits for each frame. The multiband filters are shown in each column. The top row is the Stokes Q_r image. The bottom row is Stokes I (total intensity). The apparent diameter of the disk is shown with a circle and the southern polar axis is designated with a line. Flat-field errors in the total intensity images are masked out.

Table 10

Neptune Ephemeris for 2023 July 11 Based on JPL Horizons Data

Parameter	Value
Apparent diameter	2''313
North pole angle	318°1
North pole distance	-1.''058
Sun-observer phase angle	1.°817

differencing with an adapted Mueller-matrix correction. The radial Stokes parameters, Q_r and U_r (Schmid et al. 2006), were calculated using

$$\begin{aligned} Q_r &= Q \cos(2\theta) + U \sin(2\theta) \\ U_r &= -Q \sin(2\theta) + U \cos(2\theta). \end{aligned} \quad (21)$$

For an optically thick planetary atmosphere like Neptune's, the most probable alignment of the electric field due to multiple-scattering is radially from the center of the planet to the limb; therefore, Q_r approximately equal to the polarized intensity (Schmid et al. 2006). Similar to Section 10.1, residual polarization errors were corrected with photometry, awaiting the updated instrument polarization calibration. The corrected radial Stokes Q_r frames and total intensity frames are shown in Figure 27.

The Stokes Q_r images show clear limb polarization in all filters with little polarization in the center of the image and maximum polarization at the edge. There is azimuthally symmetric polarization along the limb without significant concentrations at the poles or equator. The total intensity frames show signs of a polar cloud and mild banding structures, especially in the F720 frame. Radial profiles of Q_r , I , and Q_r/I are shown in Figure 28.

11. Conclusions

In this paper, we presented upgrades to the visible HCI polarimeter VAMPIRES. These upgrades included new detectors, coronagraphs, polarization optics, and a multiband imaging mode. We characterized the instrument and described all current optics and observing modes. A variety of engineering and science validation tests were performed, which confirmed the instrument's readiness.

We highlight key features of VAMPIRES, which emphasize its technological capabilities

1. Extreme AO and high-speed lucky imaging makes VAMPIRES capable of visible HCI, reaching angular resolutions of ~ 20 mas and Strehl ratios up to 60%.
2. Two new qCMOS detectors combine high frame rates, low read noise ($0.25e^-$ to $0.4e^-$ rms), and large format arrays with subframe readout, no cosmetic defects, and a high dynamic range (90 dB).

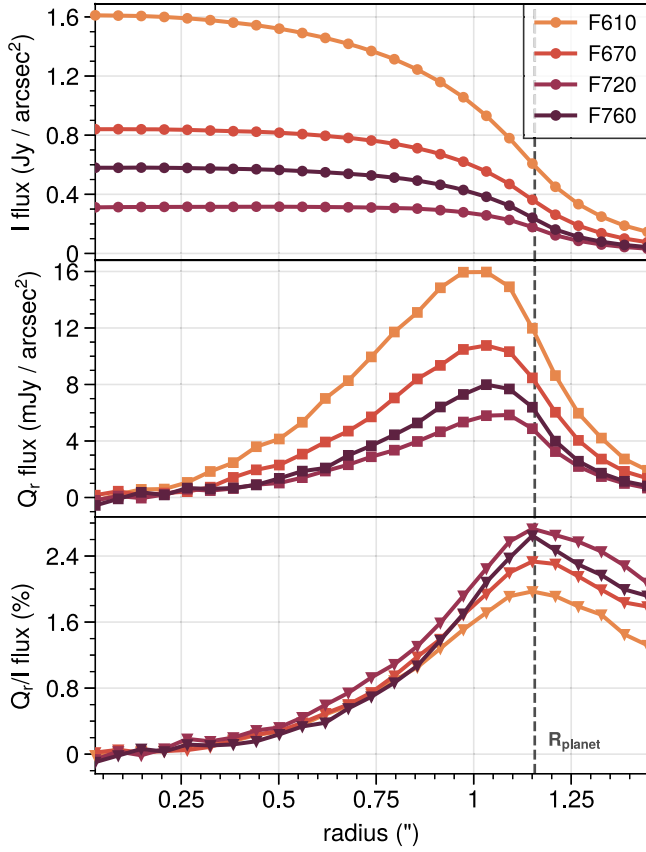


Figure 28. Radial profiles of from spectro-polarimetric observations of Neptune. All profiles use apertures 10 pixels wide. (top) Stokes I , total intensity. (middle) radial Stokes Q_r . (bottom) the ratio of the Q_r profile to the I profile.

3. We developed a dichroic-based technique for imaging multiple fields at multiple wavelengths multiplexed across the large detector arrays. This technique is compatible with many instrument modes, effectively increasing the observing efficiency by a factor of four and adding low-resolution spectral information.
4. We installed a suite of visible coronagraphs and pupil masks, enabling deep observations. Initial tests reached 5σ contrast limits of 10^{-4} – 10^{-6} from $0''.1$ to $>0''.5$.
5. Advanced polarimetric control allows significant attenuation of unpolarized signal. The new achromatic FLC has improved the polarimetric efficiency by $\sim 20\%$ and can be removed for long exposures (>1 s). Polarimetry can be incorporated into almost all observational modes of VAMPIRES, including multiband imaging.

With its technological capabilities, VAMPIRES enables the study of many interesting astrophysical phenomena and objects. In Section 10 we demonstrated VAMPIRES with

1. Spectro-polarimetric imaging of the HD 169142 circumstellar disk, detecting the inner and outer rings and measuring the wavelength dependence of the radial scattering profile
2. High-contrast SDI of the sub-stellar companion HD 1160B, measuring its astrometry and spectrum
3. Narrowband $H\alpha$ imaging of the R Aqr emission nebula, resolving the compact accretion source for the jet and discovering a new asymmetry
4. Spectro-polarimetric imaging of gas giant Neptune, confirming the limb polarization of its atmosphere and measuring the wavelength dependence of the radial scattering profile

These results highlight the utility of VAMPIRES as a visible high-contrast instrument.

11.1. Future Prospects

The most exciting prospect for VAMPIRES is commissioning the new facility adaptive optics system, AO3k (Lozi et al. 2022). This includes upgrading the 188 actuator DM to a 64×64 actuator DM, a NIR pyramid wavefront sensor (NIRWFS), and a visible nonlinear curvature wavefront sensor (nlCWFS Ahn et al. 2023). The AO3k upgrade will enable high-contrast wavefront correction directly from the facility AO, while the SCEXAO PyWFS and DM can act as a second-stage “touch-up” loop optimized for small wavefront errors and dark field control.

The NIRWFS is particularly exciting for VAMPIRES since it enables observations of very dusty, red stars. These stars are too faint in the visible for extreme AO but sufficiently bright in the NIR. Circumstellar disk hosts and young stars, in general, are perfect examples of objects optimal for taking advantage of the NIRWFS and VAMPIRES’ new long exposure capabilities. High-contrast instruments have poorly studied young and low-mass targets due to their visible faintness, and a new wave of science will be enabled by studying the disks and demographics of these systems.

While 30 m-class telescopes are still on the horizon, and their HCI instrumentation perhaps even further, instruments like SCEXAO and VAMPIRES are one the best places to develop and implement advanced technology, both software and hardware, for the next generation of ground-based high-contrast instruments: ELT/PCS (Kasper et al. 2021), TMT/PSI (Fitzgerald et al. 2019), and GMT/GMagAO-X (Kautz et al. 2023). The multi-wavelength observing techniques and wavefront control methods studied by SCEXAO today will directly apply to developing these future instruments, bringing us closer to the goals of direct imaging and characterization of planets most similar to Earth and understanding the formation pathways for planets and solar systems.

Acknowledgments

First and foremost, we wish to recognize and acknowledge the significant cultural role and reverence that the summit of Maunakea has always had within the Indigenous Hawaiian community. We are grateful and thank the community for the privilege of building instrumentation on and conducting observations from this sacred Mauna.

We thank Joshua Hacko (NH Micro), Iven Hamilton (UH), Shane Jacobson (UH/Gemini), Michael Lemmin (NAOJ), Paul Sumner (Opto-line), Lucio Ramos (NAOJ), Paul Toyoma (UH), and Matthew Wung (NAOJ) for their time and expertise in the manufacturing, assembly, testing, and integration of the VAMPIRES upgrades.

We thank Javier Alcoloa for the valuable discussions on our R Aqr observations. We thank Timothy Brandt and collaborators for the use of data obtained under Subaru proposal ID o23149. We thank Michael Fitzgerald and collaborators for the use of data obtained under Subaru proposal ID o23150. We thank telescope operators Sean Cunningham, Erin Dailey, Jonathan Laverty, Michael Letawsky, Andrew Neugarten, Larissa Schumacher, and Aidan Walk for their support during the observations used in this work. We thank the anonymous referee for useful comments which led to the improvement of this manuscript.

This research has made use of the Washington Double Star Catalog maintained at the U.S. Naval Observatory. This research was funded by the Heising-Simons Foundation through grant #2020-1823. Based on data collected at Subaru Telescope, which is operated by the National Astronomical Observatory of Japan. The development of SCEXAO is supported by the Japan Society for the Promotion of Science (Grant-in-Aid for Research #23340051, #26220704, #23103002, #19H00703, #19H00695, and #21H04998), the Subaru Telescope, the National Astronomical Observatory of Japan, the Astrobiology Center of the National Institutes of Natural Sciences, Japan, the Mt Cuba Foundation and the Heising-Simons Foundation.

Facility: Subaru (SCEXAO).

Software: ADI.jl (Lucas & Bottom 2020), AMICAL (Soulain et al. 2020), astropy (The Astropy Collaboration et al. 2013; Astropy Collaboration et al. 2018), HCIPy (Por et al. 2018), Julia (Bezanson et al. 2017), matplotlib (Hunter 2007), numpy (Harris et al. 2020), pandas (team 2024), photutils (Bradley et al. 2024), proplot (Davis 2021), pyKLIP (Wang et al. 2015), Python, showyourwork (Luger et al. 2021), scikit-image (Walt et al. 2014), synphot (STScI Development Team 2018).

Appendix A Observing Log

In Table 11 we list all observations used for this work.

Table 11
Chronologically Ordered Observing Log

Date (UTC)	Object	Filter(s)	Pol. Mode	Coron.	Pupil Mask	DIT (s)	N_{coadd}	N_{frame}	T_{exp} (min)	Seeing (")	Prop. ID
2023/06/27	Albireo	775-50	5×10^{-4}	1380	2	<1	...	o23013
2023/06/27	Albireo	Open	5×10^{-4}	3450	17	<1	...	o23013
2023/06/27	Albireo	H α /H α -Cont	0.05	300	12	1	...	o23013
2023/06/27	Albireo	S II/S II-Cont	0.03	313	21	3	...	o23013
2023/06/27	Albireo	MBI	2×10^{-3}	1000	20	5	...	o23013
2023/06/29	HD 102438	MBI	...	CLC-5	Lyot	0.01	1000	383	64	0.52 ± 0.21	o23149
2023/07/07	HD 169142	MBI	Slow	CLC-5	Lyot	1.0	10	301	50	0.83 ± 0.21	o23166
2023/07/07	HD 191195	MBI	0.03	500	5	<1	0.83 ± 0.21	o23166
2023/07/07	21 Oph	625-50	0.01	500	5	<1	0.83 ± 0.21	o23166
2023/07/07	21 Oph	675-50	0.01	500	5	<1	0.83 ± 0.21	o23166
2023/07/07	21 Oph	725-50	0.01	500	3	<1	0.83 ± 0.21	o23166
2023/07/07	21 Oph	750-50	0.01	500	5	<1	0.83 ± 0.21	o23166
2023/07/07	21 Oph	775-50	0.01	500	6	<1	0.83 ± 0.21	o23166
2023/07/07	21 Oph	Open	0.01	500	11	<1	0.83 ± 0.21	o23166
2023/07/07	HD 204827	MBI	Fast	0.01	176	52	2	0.83 ± 0.21	o23166
2023/07/07	R Aqr	H α /H α -Cont	1.2	1	348	7	0.83 ± 0.21	o23166
2023/07/10	21 Oph	MBI	0.01	500	555	46	0.56 ± 0.12	o23166
2023/07/10	HD 163296	MBI	Slow	CLC-3	Lyot	0.5	17	17	<1	0.56 ± 0.12	o23166
2023/07/11	HD 1160	MBI	...	CLC-3	Lyot	0.1	100	101	17	0.62 ± 0.14	o23166
2023/07/11	Neptune	MBI	Slow	5	1	184	15	0.62 ± 0.14	o23166
2023/07/29	HIP 3373	MBI	0.1	50	50	4	0.74 ± 0.20	o23150
2023/08/31	HR 718	625-50	7.9×10^{-5}	1000	1	<1	1.25 ± 0.39	o23013
2023/08/31	HR 718	675-50	7.9×10^{-5}	1000	1	<1	1.25 ± 0.39	o23013
2023/08/31	HR 718	725-50	7.9×10^{-5}	1000	1	<1	1.25 ± 0.39	o23013
2023/08/31	HR 718	750-50	7.9×10^{-5}	1000	1	<1	1.25 ± 0.39	o23013
2023/08/31	HR 718	775-50	7.9×10^{-5}	1000	1	<1	1.25 ± 0.39	o23013
2023/08/31	HR 718	Open	7.9×10^{-5}	1000	1	<1	1.25 ± 0.39	o23013
2023/08/31	HR 718	MBI	1.1×10^{-3}	1000	1	<1	1.25 ± 0.39	o23013
2023/08/31	HR 718	H α /H α -Cont	4.7×10^{-2}	425	1	<1	1.25 ± 0.39	o23013
2023/08/31	HR 718	S II/S II-Cont	1.1×10^{-2}	1100	1	<1	1.25 ± 0.39	o23013
2023/08/31	HD 19445	H α /H α -Cont	0.67	85	50	48	1.25 ± 0.39	o23013
2024/04/30	HD 137909	625-50	5.7×10^{-4}	500	10	<1	...	o24182
2024/04/30	HD 137909	675-50	5.7×10^{-4}	500	10	<1	...	o24182
2024/04/30	HD 137909	725-50	5.7×10^{-4}	500	10	<1	...	o24182
2024/04/30	HD 137909	750-50	5.7×10^{-4}	500	10	<1	...	o24182
2024/04/30	HD 137909	775-50	5.7×10^{-4}	500	10	<1	...	o24182
2024/04/30	HD 137909	Open	5.7×10^{-4}	500	10	<1	...	o24182
2024/04/30	HD 137909	MBI	1.6×10^{-3}	250	7	<1	...	o24182
2024/04/30	HD 139341	MBI	0.1	250	2	<1	...	o24182

Note. The number of coadds and number of frames from each data set are the average values (not all data cubes have the same number of frames). Seeing data obtained from the MKWC archive (<http://mkwc.ifa.hawaii.edu/current/seeing/index.cgi>), when available; values are the average and standard deviation DIMM measurements for the whole night.

Appendix B Instrument Models

An annotated CAD model of VAMPIRES on the visible bench of SCEXAO is shown in Figure 29.

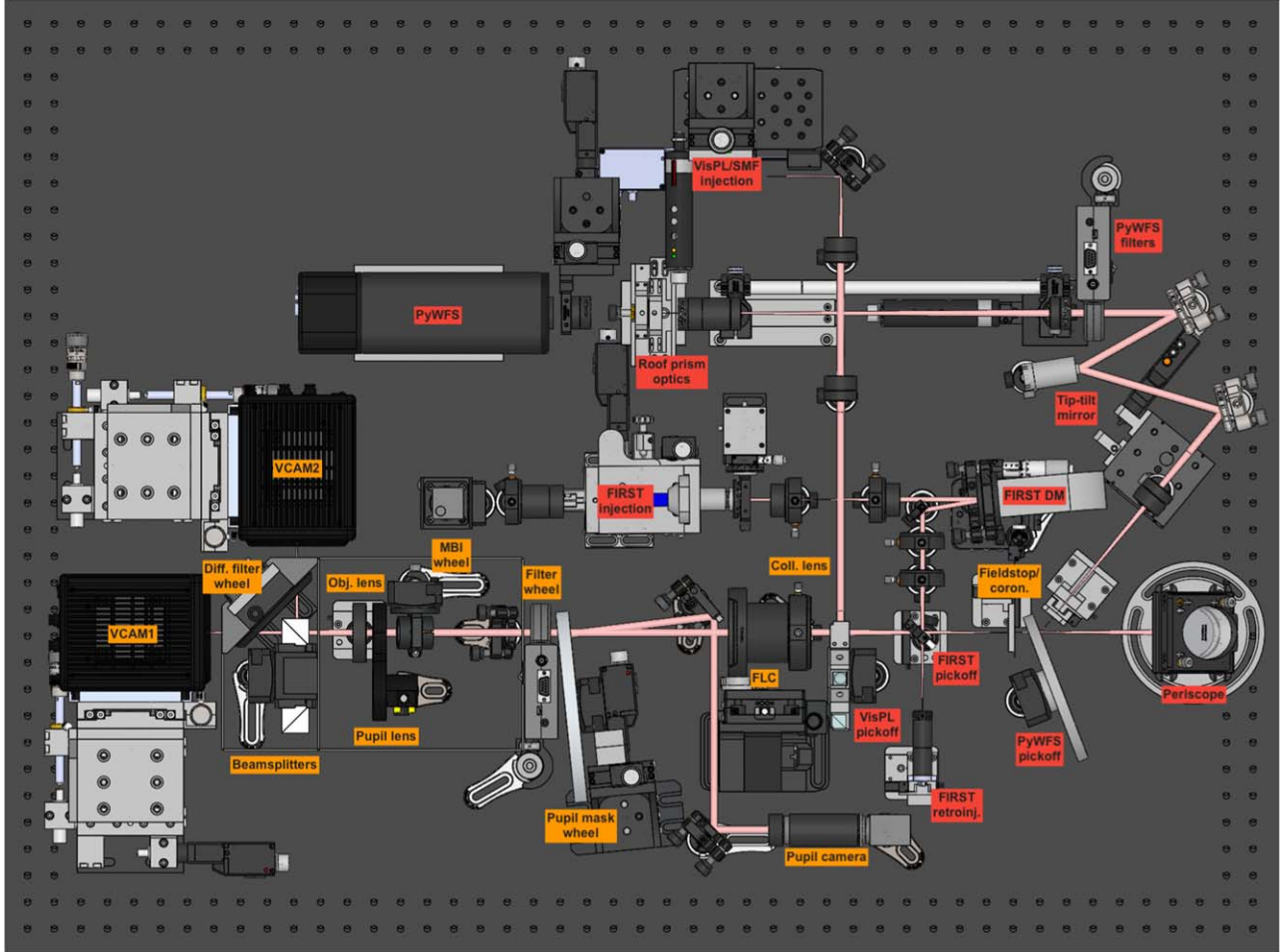


Figure 29. SCEXAO visible bench including the PyWFS, FIRST injection, and VAMPIRES. VAMPIRES optics are labeled in orange and FIRST/PyWFS optics are labeled in red. The total size of the optical table shown is 120 cm by 90 cm. Parts of the baffling around VAMPIRES optics, as well as the optical bench enclosure, are hidden for clarity.

Appendix C Photon Number Resolving Statistics

We derive the theoretical noise effects of photon-number resolving data post-hoc, wherein data that is assumed to be perfectly bias-subtracted and flat-corrected is converted to electron flux using the detector gain and rounded to the nearest whole number.

Photons that enter the detector have a certain probability of becoming photo-electrons (hereafter electrons), described by the quantum efficiency. We ignore this for now and describe

the input flux in electrons. These electrons are subject to counting statistics due to their Poisson nature. Let H be the rate of electrons per pixel (the quanta exposure). The probability of measuring a signal of k electrons is then

$$\mathcal{P}(k|H) = \frac{H^k e^{-H}}{k!}. \quad (\text{C1})$$

Now consider the Gaussian read noise, σ_{RN}

$$\mathcal{N}(x|k, \sigma_{RN}) = \frac{1}{\sigma_{RN} \sqrt{2\pi}} e^{-(x-k)^2/2\sigma_{RN}^2}. \quad (\text{C2})$$

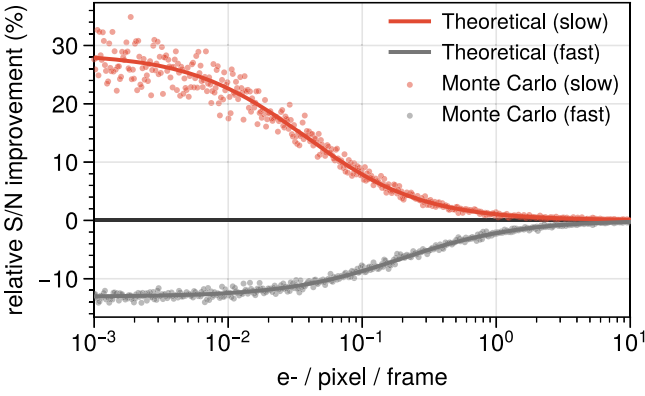


Figure 30. Relative S/N improvement from calculating the photon number via truncation in the low-flux regime compared to the standard noise terms. Solid curves are theoretical values (Equation C10) and the scatter points are Monte Carlo statistical simulations shown for both the “slow” ($\sigma_{\text{RN}} = 0.25e^-$) and the “fast” ($\sigma_{\text{RN}} = 0.4e^-$) detector readout modes.

The probability of measuring U electrons after both processes is the convolution of the two distributions

$$P(U|H, \sigma_{\text{RN}}) = \sum_{k=0}^{\infty} \mathcal{N}(U|k, \sigma_{\text{RN}}) \cdot \mathcal{P}(k|H). \quad (\text{C3})$$

Qualitatively, recognize that this can be described as discrete Poisson peaks convolved with a Gaussian of width σ_{RN} . Consider the simple case of $H=0$; the data is a Gaussian centered at zero. If this data is rounded to the nearest whole number, values $|U| > 0.5$ get rounded to -1 and 1 , respectively, or for $|U| > 1.5$ to -2 and 2 , and so on, causing variance in the measured photon number.

Consider a new distribution describing the probability of measuring values which will be rounded to the correct bins, $h(k)$

$$h(k) = P(|U - k| < 0.5 | \sigma_{\text{RN}}) \quad (\text{C4})$$

$$= \int_{k-0.5}^{k+0.5} \mathcal{N}(x|k, \sigma_{\text{RN}}) dx. \quad (\text{C5})$$

This can be rewritten using the cumulative distribution of the unit normal, Φ ,

$$h(k) = \Phi\left(\frac{k+0.5}{\sigma_{\text{RN}}}\right) - \Phi\left(\frac{k-0.5}{\sigma_{\text{RN}}}\right) \quad (\text{C6})$$

with

$$\Phi(z) = \frac{1}{2} \left[1 - \operatorname{erf}\left(\frac{z}{\sqrt{2}}\right) \right], \quad (\text{C7})$$

where erf is the error function.

The expected value of this distribution is 0 by convenience of symmetry

$$E[h] = \sum_{k=-\infty}^{\infty} k \cdot h(k) = 0, \quad (\text{C8})$$

and the variance of this distribution is

$$\operatorname{Var}[h] = \sum_{k=-\infty}^{\infty} k^2 \cdot h(k). \quad (\text{C9})$$

For practical applications, k is truncated to ± 5 since the probability of observing a Gaussian event over five standard deviations away is extremely small, below 10^{-5} , and thus $h(k) \approx 0$.

Therefore, the total noise from photon number resolving is the combination of photon noise and Equation C9–

$$\sigma = \sqrt{U + \sum_{k=-\infty}^{\infty} k^2 \cdot \left[\Phi\left(\frac{k+0.5}{\sigma_{\text{RN}}}\right) - \Phi\left(\frac{k-0.5}{\sigma_{\text{RN}}}\right) \right]}. \quad (\text{C10})$$

In Figure 30, the relative improvement in S/N by photon number resolving (i.e., converting the signal to electrons and rounding to the nearest whole number) is shown. We also show the standard deviation of Monte Carlo samples ($N = 10^4$) with and without rounding to confirm our theoretical results. Note that there are more sophisticated algorithms for achieving higher S/N ratios with photon-number resolving than simply rounding after the fact (see Harpsøe et al. 2012), but this is still a somewhat contrived use case for a ground-based instrument like VAMPIRES, which will be photon-noise limited for most observations.

Appendix D Multiband Imaging Ghosts

When stacking dichroics with low angles of incidence, extra reflections create ghost PSFs. Our multiband dichroic technique (Section 2.4) uses three dichroics in front of a mirror with $\sim 0.4^\circ$ tilts between each filter with respect to the mirror. We characterized the ghost PSFs using a dispersing prism to understand their origin by analyzing spectra.

To explain, consider the simple case of a single dichroic with a tilt, θ , in front of a mirror (Figure 31). There are three rays to explain the ghost behavior—the first is the light reflected by the dichroic (green arrow), which has an angle of -2θ . The second ray is transmitted through the dichroic, reflects off the mirror, and returns with an angle of 0° (solid blue arrow). Because the dichroic has parallel faces, there is no angular deviation of the transmitted rays. The angle between the solid blue and green arrows (2θ) is the characteristic separation between the fields in the focal plane.

The final ray is formed from a transmitted beam that reflects off the rear mirror and then off the dichroic’s backside (dashed

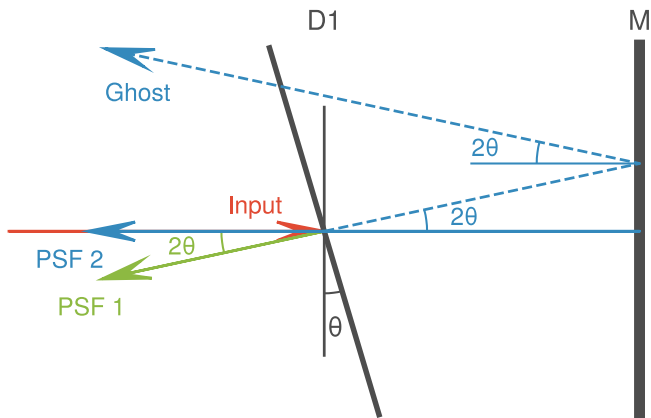


Figure 31. Raytrace diagram for ghosts from stacked dichroics. D1 represents a dichroic tilted at angle θ , and M represents a standard mirror. The incoming ray (red arrow) goes from left to right. The light reflected by D1 is shown with a green arrow. Light transmitted by D1 is blue—the solid line is the main ray and the dashed line is the first ghost ray.

blue arrow). The reflection is a natural consequence of the dichroic filter curve—any light that is not fully transmitted will be reflected by the dielectric coating and return towards the mirror, picking up an angle of 2θ due to the tilt of the dichroic. This beam reflects off the rear mirror again and then is transmitted through the dichroic with a ray angle of 2θ . This will form a PSF with the same spectrum as “PSF 2” but separated by an angle of 2θ . More back reflections can occur every time the light transmits through the dichroic, reflecting a small fraction of the light at integer multiple separations of 2θ (i.e., 4θ , 6θ , and so on). These higher-order ghosts are less concerning because they are exponentially fainter and far from the primary PSFs.

One way to remove these ghosts would be to improve the dielectric coatings of the filters until the ghosts are undetectable. Our multiband dichroics have a transmission of $\sim 95\%$ outside of the OD = 4 blocking region, meaning $\sim 5\%$ of light is reflected into these ghosts and easily detected. It is difficult and expensive to manufacture dichroics that simultaneously have efficient blocking (OD > 3) in band and high throughput out of band ($>99.9\%$), so we opted to address the ghosts geometrically creating a focal plane layout where no ghosts overlap with any science fields.

Our solution uses optimal angles for the dichroic tilts which place any ghost PSFs (and their $3''$ FOV) completely out of the FOV of the primary fields (Figure 32). Our design uses as few pixel rows as possible to maximize detector readout speed. Additionally, a single field can be cropped out to double the readout speed leaving three fields remaining. For the final design, angles were chosen for each dichroic slightly larger than $3''$ so that the manufacturing tolerances would allow for at least ~ 10 px between fields.

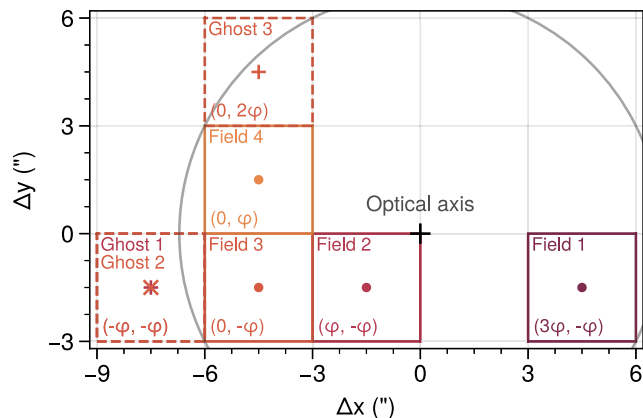


Figure 32. Diagram of the fields produced by the VAMPIRES multiband dichroics. Each field is colored based on the expected spectrum, from brown (F760) to orange (F610). Each field is labeled in the bottom left with the angular displacement (x, y) of the field in terms of $\varphi = 2\theta$, the magnified angle offset between dichroic filters in the MBI stack.

Appendix E.

Measuring the Non-telecentricity of VAMPIRES

VAMPIRES is non-telecentric, which means that a shift in focus affects the plate scale in the detector plane. Given the instrument’s space constraints, this is nearly impossible to avoid optically. In theory, if the instrument F-ratio is stable and the detector is reasonably well-focused, then the plate scale should stay stable. Nonetheless, we quantify the change in plate scale as a function of defocus using the SCEXAO internal pinhole mask.

For this experiment, we used the pinhole mask and moved the detector stage in steps around the optimal focus. For each frame, PSFs were fit to the pinhole grid, and the average

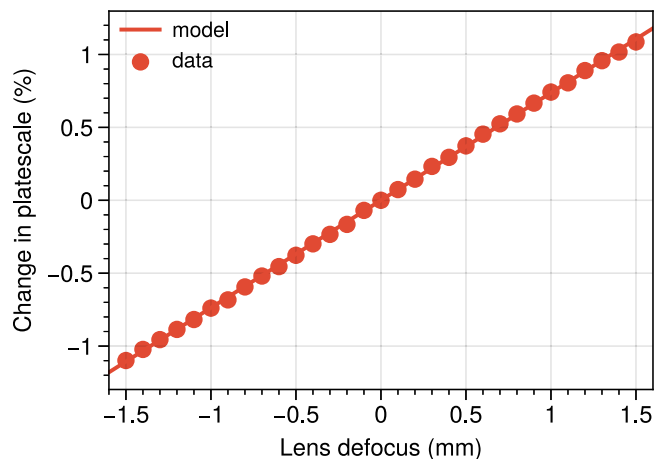


Figure 33. The percentage change in plate scale as the image passes through focus due to the non-telecentricity of the optical system. A linear model is fit to the data and shown with a solid line.


separation was calculated. The relative displacement of the grid as a function of defocus is shown in Figure 33.

These data were fit with a linear model correlating the percentage change in plate scale to the absolute defocus in mm. The fit is shown in Figure 33 which has a slope of $(1.106 \pm 0.003)\% \text{ mm}^{-1}$. This means the objective lens must stay focused to better than 0.09 mm precision to keep the astrometric precision below 0.1%, which is not difficult to achieve when focusing with the internal laser.

Appendix F Data and Code Availability

This study used the reproducibility software `showyourwork` (Luger et al. 2021), which leverages continuous integration to create the figures and compile this manuscript programmatically. Each figure caption contains a link to the script used to make the figure (at the commit corresponding to the current build of the manuscript). The git repository associated with this study is publicly available at https://github.com/mileslucas/vampires_instrument_paper. Reduced data is available upon request, and raw observational data is available from the SMOKA archive.²⁵

ORCID iDs

Miles Lucas  <https://orcid.org/0000-0001-6341-310X>
 Barnaby Norris  <https://orcid.org/0000-0002-8352-7515>
 Olivier Guyon  <https://orcid.org/0000-0002-1097-9908>
 Michael Bottom  <https://orcid.org/0000-0003-1341-5531>
 Vincent Deo  <https://orcid.org/0000-0003-4514-7906>
 Sébastien Vievard  <https://orcid.org/0000-0003-4018-2569>
 Julien Lozi  <https://orcid.org/0000-0002-3047-1845>
 Kyohoon Ahn  <https://orcid.org/0000-0002-1094-852X>
 Jaren Ashcraft  <https://orcid.org/0000-0001-5082-7442>
 Thayne Currie  <https://orcid.org/0000-0002-7405-3119>
 David Doelman  <https://orcid.org/0000-0003-0695-0480>
 Tomoyuki Kudo  <https://orcid.org/0000-0002-9294-1793>
 Lucie Leboulleux  <https://orcid.org/0000-0002-8566-2577>
 Lucinda Lilley  <https://orcid.org/0009-0009-6274-6514>
 Maxwell Millar-Blanchaer  <https://orcid.org/0000-0001-6205-9233>
 Boris Safonov  <https://orcid.org/0000-0003-1713-3208>
 Peter Tuthill  <https://orcid.org/0000-0001-7026-6291>
 Taichi Uyama  <https://orcid.org/0000-0002-6879-3030>
 Aidan Walk  <https://orcid.org/0009-0005-0321-0104>
 Manxuan Zhang  <https://orcid.org/0000-0003-3567-6839>

References

Ahn, K., Guyon, O., Lozi, J., et al. 2021, *Proc. SPIE*, 11823, 1182303
 Ahn, K., Guyon, O., Lozi, J., et al. 2023, in *Adaptive Optics for Extremely Large Telescopes (AO4ELT7)*, 73

Alcolea, J., Mikołajewska, J., Gómez-Garrido, M., et al. 2023, in *Highlights on Spanish Astrophysics XI (Sociedad Española de Astronomía)*, ed. M. Manteiga et al., 190
 Astropy Collaboration, Price-Whelan, A. M., Sipőcz, B. M., et al. 2018, *AJ*, 156, 123
 Bailey, J., Cotton, D. V., De Horta, A., Kedziora-Chudczer, L., & Shastri, O. 2023, *MNRAS*, 520, 1938
 Bailey, J., Cotton, D. V., Kedziora-Chudczer, L., De Horta, A., & Maybour, D. 2020, *PASA*, 37, e004
 Bailey, J., Cotton, D. V., & Kedziora-Chudczer, L. 2017, *MNRAS*, 465, 1601
 Bailey, J., Kedziora-Chudczer, L., Cotton, D. V., et al. 2015, *MNRAS*, 449, 3064
 Benisty, M., Bae, J., Facchini, S., et al. 2021, *ApJL*, 916, L2
 Benisty, M., Dominik, C., Follette, K., et al. 2023, in *Protostars and Planets VII*, 534, *Astronomical Society of the Pacific Conference Series*, ed. S. Inutsuka et al., 605
 Bertrang, G. H.-M., Avenhaus, H., Casassus, S., et al. 2018, *MNRAS*, 474, 5105
 Bessell, M. S. 1979, *PASP*, 91, 589
 Beuzit, J.-L., Vigan, A., Mouillet, D., et al. 2019, *A&A*, 631, A155
 Bezanson, J., Edelman, A., Karpinski, S., & Shah, V. B. 2017, *SIAMR*, 59, 65
 Blunt, S., Nielsen, E. L., De Rosa, R. J., et al. 2017, *AJ*, 153, 229
 Boer, J. d., Langlois, M., Holstein, R. G. v., et al. 2020, *A&A*, 633, A63
 Bottom, M., Ruane, G., & Mawet, D. 2017, *RNAAS*, 1, 30
 Bowler, B. P., Blunt, S. C., & Nielsen, E. L. 2020, *AJ*, 159, 63
 Bradley, L., Sipőcz, B., Robitaille, T., et al. 2024, *astropy/photutils: v1.13.0*, Zenodo, doi:10.5281/zenodo.12585239
 Bujarrabal, V., Alcolea, J., Mikołajewska, J., Castro-Carrizo, A., & Ramstedt, S. 2018, *A&A*, 616, L3
 Buton, C., Copin, Y., Aldering, G., et al. 2013, *A&A*, 549, A8
 Chen, M., Wang, J. J., Brandt, T. D., et al. 2023, *RASTI*, 2, 620
 Christiaens, V., Gonzalez, C. A. G., Farkas, R., et al. 2023, *JOSS*, 8, 4774
 Close, L. M., Males, J. R., Follette, K. B., et al. 2014, *Proc. SPIE*, 9148, 580
 Currie, T., Biller, B., Lagrange, A., et al. 2023, in *Protostars and Planets VII*, 534, ed. S. Inutsuka (San Francisco: ASP), 799
 Currie, T., Kasdin, N. J., Groff, T. D., et al. 2018, *PASP*, 130, 044505
 Currie, T., Lawson, K., Schneider, G., et al. 2022, *NatA*, 6, 751
 Davis, L. L. B. 2021, *ProPlot v0.9.5.post360*, Zenodo, doi:10.5281/zenodo.5602155
 Docobo, J. A., & Ling, J. F. 2007, *IAUDS*, 161, 1
 Docobo, J. A., & Ling, J. F. 2017, *IAU Double Star Information Circular 192*, Tech. Rep. 192, <http://www.astro.gsu.edu/wds/bsl/cir192.pdf>
 Doelman, D. S., Belaouchi, H., Riggs, A. J., et al. 2023, in *Proc. SPIE*, 12680 (Techniques and Instrumentation for Detection of Exoplanets XI)
 Drimmel, R., Sozzetti, A., Schröder, K.-P., et al. 2021, *MNRAS*, 502, 328
 Egner, S., Ikeda, Y., Watanabe, M., et al. 2010, *Proc. SPIE*, 7736, 77364V
 Escorza, A., Karinkuzhi, D., Jorissen, A., et al. 2019, *A&A*, 626, A128
 Fedele, D., Carney, M., Hogerheijde, M. R., et al. 2017, *A&A*, 600, A72
 Fitzgerald, M., Bailey, V., Baranec, C., et al. 2019, *BAAS*, 51, 251
 Fried, D. L. 1966, *JOSA*, 56, 1372
 Gaia Collaboration, Brown, A. G. A., Vallenari, A., et al. 2018, *A&A*, 616, A1
 Gaia Collaboration, Brown, A. G. A., Vallenari, A., et al. 2021, *A&A*, 649, A1
 Gaia Collaboration, Prusti, T., de Bruijne, J. H. J., et al. 2016, *A&A*, 595, A1
 Galicher, R., & Mazoyer, J. 2024, *CRPhy*, 24, 133
 Garcia, E. V., Currie, T., Guyon, O., et al. 2017, *ApJ*, 834, 162
 Garrel, V., Guyon, O., & Baudoz, P. 2012, *PASP*, 124, 861
 Gomez Gonzalez, C. A., Wertz, O., Absil, O., et al. 2017, *AJ*, 154, 7
 Gordon, K. D., Bohlin, R., Sloan, G. C., et al. 2022, *AJ*, 163, 267
 Groff, T. D., Kasdin, N. J., Limbach, M. A., et al. 2015, *Proc. SPIE*, 9605, 457
 Gromadzki, M., & Mikołajewska, J. 2009, *A&A*, 495, 931
 Guyon, O. 2018, *ARA&A*, 56, 315
 Hammond, I., Christiaens, V., Price, D. J., et al. 2023, *MNRAS: Letters*, 522, L51
 Hamuy, M., Suntzeff, N. B., Heathcote, S. R., et al. 1994, *PASP*, 106, 566
 Hamuy, M., Walker, A. R., Suntzeff, N. B., et al. 1992, *PASP*, 104, 533
 Harpsøe, K. B. W., Andersen, M. I., & Kjægaard, P. 2012, *A&A*, 537, A50
 Harrington, D., Berdyugina, S., Chun, M., et al. 2014, *Proc. SPIE*, 9147, 91477C
 Harris, C. R., Millman, K. J., van der Walt, S. J., et al. 2020, *Natur*, 585, 357
 Hinkle, K. H., Brittain, S., Fekel, F. C., Lebzelter, T., & Boogert, A. 2022, *ApJ*, 937, 98

²⁵ <https://smoka.nao.ac.jp/>

- Holstein, R. G. v., Girard, J. H., Boer, J. d., et al. 2020, *A&A*, 633, A64
- Hunter, J. D. 2007, *CSE*, 9, 90
- Hunziker, S., Schmid, H. M., Mouillet, D., et al. 2020, *A&A*, 634, A69
- Izmailov, I. S. 2019, *AstL*, 45, 30
- Janesick, J. R. 2007, Photon Transfer (SPIE: Bellingham, WA)
- Joost't Hart, G. J., van Holstein, R. G., Bos, S. P., et al. 2021, in Proc. SPIE, 11833 (Polarization Science and Remote Sensing X)
- Jovanovic, N., Guyon, O., Martinache, F., et al. 2015a, *ApJL*, 813, L24
- Jovanovic, N., Martinache, F., Guyon, O., et al. 2015b, *PASP*, 127, 890
- Kasper, M., Cerpa Urta, N., Pathak, P., et al. 2021, *The Messenger*, 182, 38
- Kautz, M., Males, J. R., Close, L. M., et al. 2023, in Adaptive Optics for Extremely Large Telescopes (AO4ELT7), 61
- Kemp, J. C. 1969, *JOSA*, 59, 950
- Kooten, M. A. M. v., & Izett, J. G. 2022, *PASP*, 134, 95001
- Kuhn, J. R., Potter, D., & Parise, B. 2001, *ApJL*, 553, L189
- Labeyrie, A., Lipson, S. G., & Nisenson, P. 2014, An Introduction to Optical Stellar Interferometry (Cambridge: Cambridge Univ. Press)
- Lang, D., Hogg, D. W., & Mykytyn, D. 2016, Astrophysics Source Code Library, ascl:1604.008
- Law, N. M., Mackay, C. D., & Baldwin, J. E. 2006, *A&A*, 446, 739
- Lebouilleux, L., Carlotti, A., N'Diaye, M., et al. 2022, *A&A*, 666, A91
- Lebouilleux, L., Guyon, O., Lozi, J., et al. 2024, *Proc. SPIE*, 13097, 130973G
- Lozi, J., Ahn, K., Clergeon, C., et al. 2022, *Proc. SPIE*, 12185, 1218533
- Lozi, J., Guyon, O., Kudo, T., et al. 2020a, *Proc. SPIE*, 11448, 114487C
- Lozi, J., Guyon, O., Vievard, S., et al. 2020b, *Proc. SPIE*, 11448, 114480N
- Lozi, J., Jovanovic, N., Guyon, O., et al. 2019, *PASP*, 131, 044503
- Lucas, M., & Bottom, M. 2020, *JOSS*, 5, 2843
- Lucas, M., Bottom, M., Guyon, O., et al. 2022, *Proc. SPIE*, 12184, 121844E
- Luger, R., Bedell, M., Foreman-Mackey, D., et al. 2021, arXiv:2110.06271
- Maire, A.-L., Bonnefoy, M., Ginski, C., et al. 2016, *A&A*, 587, A56
- Males, J. R., Close, L. M., Haffert, S., et al. 2022, *Proc. SPIE*, 12185, 1218509
- Males, J. R., Close, L. M., Haffert, S. Y., et al. 2024, *Proc. SPIE*, 13097, 1309709
- Mattioli, M., Pedichini, F., Antonucci, S., et al. 2018, *Proc. SPIE*, 10702, 107024F
- Mawet, D., Milli, J., Wahhaj, Z., et al. 2014, *ApJ*, 792, 97
- McClure, R. D., Fletcher, J. M., & Nemeč, J. M. 1980, *ApJL*, 238, L35
- Merrill, P. W. 1935, *ApJ*, 81, 351
- Merrill, P. W. 1940, Spectra of Long-period Variable Stars (Chicago, IL: Univ. Chicago Press)
- Mesa, D., D'Orazi, V., Vigan, A., et al. 2020, *MNRAS*, 495, 4279
- Miles, K., & Mason, B. 2017, IAU double star information circular 191, Tech. Rep. 191, <http://www.astro.gsu.edu/wds/bsl/cir191.pdf>
- Milli, J., Kasper, M., Bourget, P., et al. 2018, *Proc. SPIE*, 10703, 752
- Minowa, Y., Hayano, Y., Oya, S., et al. 2010, *Proc. SPIE*, 7736, 77363N
- Monnier, J. D., Harries, T. J., Aarnio, A., et al. 2017, *ApJ*, 838, 20
- Monnier, J. D., Harries, T. J., Bae, J., et al. 2019, *ApJ*, 872, 122
- Muterspaugh, M. W., Hartkopf, W. I., Lane, B. F., et al. 2010, *AJ*, 140, 1623
- N'Diaye, M., Dohlen, K., Fusco, T., & Paul, B. 2013, *A&A*, 555, A94
- Nielsen, E. L., Liu, M. C., Wahhaj, Z., et al. 2012, *ApJ*, 750, 53
- Norris, B., Schworer, G., Tuthill, P., et al. 2015, *MNRAS*, 447, 2894
- Pairat, B., Cantalloube, F., Gomez Gonzalez, C. A., et al. 2019, *MNRAS*, 487, 2262
- Pairat, B., Cantalloube, F., & Jacques, L. 2020, *MNRAS*, 503, 3724
- Perin, M. D., Duchene, G., Millar-Blanchaer, M., et al. 2015, *ApJ*, 799, 182
- Pickles, A. J. 1998, *PASP*, 110, 863
- Pohl, A., Benisty, M., Pinilla, P., et al. 2017, *ApJ*, 850, 52
- Por, E. H., Haffert, S. Y., Radhakrishnan, V. M., et al. 2018, *Proc. SPIE*, 10703, 1070342
- Pueyo, L. 2016, *ApJ*, 824, 117
- Quanz, S. P., Avenhaus, H., Buenzli, E., et al. 2013, *ApJL*, 766, L2
- Roberts, L. C., Jr, Perrin, M. D., Marchis, F., et al. 2004, *Proc. SPIE*, 5490, 504
- Roddier, F. 1981, *PrOpt*, 19, 281
- Rodenhuis, M., Canovas, H., Jeffers, S. V., et al. 2012, *Proc. SPIE*, 8446, 84469I
- Roth, K. C., Smith, A., Stephens, A., & Smirnova, O. 2016, *Proc. SPIE*, 9910, 99101B
- Sacchi, A., Karovska, M., Raymond, J., et al. 2024, *ApJ*, 961, 12
- Safonov, B. S., Lysenko, P. A., & Dodin, A. V. 2017, *AstL*, 43, 344
- Sahoo, A., Guyon, O., Lozi, J., et al. 2020, *AJ*, 159, 250
- Schmid, H. M., Bazzon, A., Milli, J., et al. 2017, *A&A*, 602, A53
- Schmid, H. M., Bazzon, A., Roelfsema, R., et al. 2018, *A&A*, 619, A9
- Schmid, H. M., Joos, F., & Tschan, D. 2006, *A&A*, 452, 657
- Soulain, A., Sivaramakrishnan, A., Tuthill, P., et al. 2020, *Proc. SPIE*, 11446, 1144611
- Soumerai, R., Ferrari, A., Aime, C., & Jolissaint, L. 2007, *ApJ*, 669, 642
- Soumerai, R., Pueyo, L., & Larkin, J. 2012, *ApJL*, 755, L28
- Stapper, L. M., & Ginski, C. 2022, *A&A*, 668, A50
- Starkey, D. A., & Fossum, E. R. 2016, *IEEE Journal of the Electron Devices Society*, 4, 129
- Stefanov, K. D. 2022, CMOS Image Sensors (Bristol, UK: IOP Publishing)
- Steiger, S., Brandt, T. D., Guyon, O., et al. 2022, *AJ*, 164, 186
- Stone, R. P. S. 1996, *ApJS*, 107, 423
- Strakhov, I. A., Safonov, B. S., & Cheryasov, D. V. 2023, *AstBu*, 78, 234
- STScI Development Team 2018, synphot: Synthetic Photometry Using Astropy, Astrophysics Source Code Library, ascl:1811.001
- team, T. p. d. 2024, pandas v2.0.3, Zenodo, doi:10.5281/zenodo.10957263
- The Astropy Collaboration, Robitaille, T. P., Tollerud, E. J., et al. 2013, *A&A*, 558, A33
- Tinbergen, J. 2005, Astronomical Polarimetry (Cambridge: Cambridge Univ. Press)
- Tinbergen, J. 2007, *PASP*, 119, 1371
- Tuthill, P. G., Monnier, J. D., & Danchi, W. C. 2000, *Proc. SPIE*, 4006, 491
- Uyama, T., Norris, B., Jovanovic, N., et al. 2020, *JATIS*, 6, 045004
- Uyama, T., Takami, M., Cugno, G., et al. 2022, *AJ*, 163, 268
- van Holstein, R. G., Keller, C. U., Snik, F., & Bos, S. P. 2023, *AAP*, 677, A150
- Vernazza, P., Ferrais, M., Jorda, L., et al. 2021, *A&A*, 654, A56
- Vievard, S., Huby, E., Lacour, S., et al. 2023a, *A&A*, 677, A84
- Vievard, S., Lallement, M., Huby, E., et al. 2023b, *Proc. SPIE*, 12680, 126800H
- Walt, S. v. d., Schönberger, J. L., Nunez-Iglesias, J., et al. 2014, *PeerJ*, 2, e453
- Wang, J. J., Ruffio, J.-B., De Rosa, R. J., et al. 2015, Astrophysics Source Code Library, ascl:1506.001
- Watanabe, M., Pyo, T.-S., Terada, H., et al. 2018, *Proc. SPIE*, 10702, 107023V
- Zacharias, N., Finch, C., & Frouard, J. 2017, *AJ*, 153, 166
- Zacharias, N., Finch, C. T., Girard, T. M., et al. 2013, *AJ*, 145, 44
- Zhang, M., Millar-Blanchaer, M., Safonov, B., et al. 2023, *Proc. SPIE*, 12680, 126800S